Structural basis of EHEP-mediated offense against phlorotannin-induced defense from brown algae to protect *aku*BGL activity

Xiaomei Sun[1,¶], Yuxin Ye[1,#a,¶], Naofumi Sakurai[1], Hang Wang[1], Koji Kato[1,#b], Jian Yu[1], Keizo Yuasa[2,#c], Akihiko Tsuji[2], Min Yao[1,*]

[1] Faculty of Advanced Life Science, Hokkaido University, Sapporo, Japan

[2] Graduate School of Bioscience and Bioindustry, Tokushima University, Tokushima, Japan

[#a] Current address: Pingshan translational medicine center, Shenzhen Bay Laboratory, Shenzhen, China

[#b] Current address: Structural Biology Division, Japan Synchrotron Radiation Research Institute (JASRI), Hyogo, Japan

[#c] Current address: Faculty of Science and Engineering, Setsunan University, Neyagawa, Japan

*Corresponding author

E-mail: yao@castor.sci.hokudai.ac.jp (MY)

¶ These authors contributed equally to this work.

Abstract

The defensive-offensive associations between algae and herbivores determine marine ecology. Brown algae utilize phlorotannin as their chemical defense against the predator *Aplysia kurodai*, which uses β-glucosidase (*aku*BGL) to digest the laminarin in algae to glucose. Moreover, *A. kurodai* employs *Eisenia* hydrolysis-enhancing protein (EHEP) as an offense to protect *aku*BGL activity from phlorotannin inhibition by precipitating phlorotannin. To underpin the molecular mechanism of this digestive-defensive-offensive system, we determined the structures of apo and tannic-acid (TNA, a phlorotannin-analog) bound form of EHEP, as well as apo *aku*BGL. EHEP consisted of three peritrophin-A domains formed in a triangle and bound TNA in the center without significant conformational changes. Structural comparison between EHEP and EHEP–TNA led us to find that EHEP can be resolubilized from phlorotannin-precipitation at an alkaline pH, which reflects a requirement in the digestive tract. *aku*BGL contained two GH1 domains, only one of which conserved the active site. Combining docking analysis, we propose the mechanisms by which phlorotannin inhibits *aku*BGL by occupying the substrate-binding pocket, and EHEP protects *aku*BGL against the inhibition by binding with phlorotannin to free the *aku*BGL pocket.

Introduction

Over millions of years of evolution, predators have successfully coevolved with their prey to maintain an ecological balance [1]. In marine habitats, interactions between algae and marine herbivores dominate marine ecosystems. Most algae are consumed by marine herbivores [2]. They produce secondary metabolites as a chemical defense to protect themselves against predators. In brown algae *Eisenia bicyclis*, laminarin is a major storage carbohydrate, constituting 20%–30% of algae dry weight. The sea hare *Aplysia kurodai*, a marine gastropod, preferentially feeds on the *E. bicyclis* with its 110 and 210 kDa β-glucosidases (*aku*BGLs), hydrolyzing the laminarin and releasing large amounts of glucose. Interestingly, such a feeding strategy has attracted attention for producing glucose as a renewable biofuel source [3]. However, to protect themselves against predators, brown algae produce phlorotannin, a secondary metabolite, thereby reducing the digestion by *A. kurodai* by inhibiting the hydrolytic activity of *aku*BGLs. As the 110 kDa *aku*BGL is more sensitive to phlorotannin than the 210 kDa BGL [4], we focused on the 110 kDa *aku*BGL in this study (hereafter, *aku*BGL refers to 110 kDa *aku*BGL).

To counteract the antipredator adaptations of algae, herbivores use diverse approaches, such as detoxification, neutralization, defense suppression, and physiological adaptations [5]. *A. kurodai* inhibits the phlorotannin-defense of brown algae through *Eisenia* hydrolysis-enhancing protein (EHEP), a protein from their digestive system that protects *aku*BGL activity from phlorotannin inhibition [4]. Previous studies have shown that incubating *E. bicyclis* with *aku*BGL in the presence of EHEP results in increased glucose production because EHEP binds to phlorotannin and forms an insoluble complex [4].

The *aku*BGL–phlorotannin/laminarin–EHEP system exemplifies the digestion process of *A. kurodai* as well as the defense and antidefense strategies between *E. bicyclis* and *A. kurodai*. Although the defense/antidefense strategy has been established,

63 the detailed molecular mechanism of this interplay remains unknown. Further,
64 phlorotannin inhibition hinders the potential application of brown algae as feedstocks
65 for enzymatically producing biofuel from laminarin. Thus, understanding the
66 underlying molecular mechanisms will be beneficial for the application of this system
67 in the biofuel industry.

68 Despite the potential use of laminarin hydrolytic enzymes in the biofuel industry,
69 only a few BGLs of glycoside hydrolases belonging to the GH3 and GH1 family are
70 known to hydrolyze laminarin (e.g., *Talaromyces amestolkiae* BGL[6], *Ustilago*
71 *esculenta* BGL [7], and V*ibrio campbellii* BGL [8] from the GH3 family and
72 *Saccharophagus degradans* 2-40^{T} BGL [9] from the GH1 family). GH3 is a multidomain
73 enzyme family characterized by N-terminal $(\beta/\alpha)_8$ (NTD) and C-terminal $(\beta/\alpha)_6$ (CTD)
74 domains, with or without auxiliary domains [10]; the nucleophile aspartate and the
75 acid/base glutamate residues exist in the NTD and CTD, respectively. In contrast, the
76 members of the GH1 family generally share a single $(\beta/\alpha)_8$-fold domain (hereafter
77 referred to as GH1 domain [GH1D]), and the two glutamic acid catalytic residues are
78 located in the carboxyl termini of β-strands 4 and 7. Therefore, the two families may
79 use different substrate-recognition and catalytic mechanisms for laminarin. Intriguingly,
80 although *aku*BGL possesses laminarin hydrolytic activity and belongs to the GH1
81 family, its molecular weight is considerably greater than that of other GH1 members.
82 Sequence analysis has indicated that *aku*BGL consists of ≥2 GH1Ds. Because no
83 structural information of BGL active on polysaccharides is available, the catalytic
84 mechanism toward laminarin is unclear.

85 There is limited information on EHEP, a novel cysteine-rich protein (8.2% of the
86 amino acid content), because no structural or functional homologous protein exists in
87 other organisms. EHEP was predicted to consist of three peritrophin-A domains (PADs)
88 with a cysteine-spacing pattern of $CX_{15}CX_5CX_9CX_{12}CX_{5\text{-}9}C$. The PADs consist of
89 peritrophic matrix proteins, which have been proposed to play an important role in
90 detoxifying ingested xenobiotics [11]. For instance, *Aedes aegypti* intestinal mucin 1

91 (*Ae*IMUC1) consists of a signal peptide followed by three PADs with an intervening
92 mucin-like domain; its expression is induced by blood feeding. *Ae*IMUC1-mediated
93 blood detoxification during digestion is completed by binding to toxic heme molecules
94 [12]. Despite the similar domain organization of EHEP and *Ae*IMUC1, their function and
95 binding partner are completely different, implying their different characteristics.
96 However, the characteristics of the EHEP-phlorotannin insoluble complex remain
97 unknown; moreover, it remains unclear why and how EHEP protects *aku*BGL from
98 phlorotannin inhibition.

99 In this study, we determined the structures of apo and tannic acid (TNA,
100 phlorotannin-analog) bound-form of EHEP (EHEP, EHEP–TNA), as well as *aku*BGL;
101 all isolated from *A. kurodai*. The structure of EHEP consists of three PADs arranged in
102 a triangle shape, with TNA bound at the surface of the triangle center. A structural
103 comparison of EHEP and EHEP–TNA revealed no significant changes in conformation
104 upon TNA binding, implying that EHEP maintains its structure when precipitated with
105 TNA. Then, we found the conditions to resolubilize EHEP–TNA precipitate for EHEP
106 recycling. The obtained *aku*BGL structure suggests that only one GH1D (GH1D2)
107 possesses laminarin hydrolytic activity; subsequently, ligand-docking experiments
108 demonstrated that TNA/phlorotannin has a higher docking score than laminarin. Our
109 results revealed the mechanisms by which EHEP protects *aku*BGL from phlorotannin
110 inhibition and phlorotannin inhibits the hydrolytic activity of *aku*BGL, providing
111 structural support for the potential application of brown algae for biofuel production.

112 Results

113 Effects of TNA on *aku*BGL activity with or without EHEP

114 Phlorotannin, a type of tannin, is a chemical defense metabolite of brown algae. It
115 is difficult to isolate a compound from phlorotannins because they are a group of

116 polyphenolic compounds with different sizes and varying numbers of phloroglucinol
117 units [13], such as eckol, dieckol, and so on [14]. Previous studies have reported that the
118 phlorotannin-analog TNA has a comparable inhibition effect on *aku*BGL to that of
119 phlorotannin [4]. Hence, we used TNA instead of a phlorotannin to explore phlorotannin
120 binding with EHEP and *aku*BGL. This activity assay system involves multiple
121 equilibration processes: *aku*BGL⇋substrate, *aku*BGL⇋TNA, and EHEP ⇋TNA. First,
122 we confirmed TNA inhibition of *aku*BGL activity and clarified the protective effects of
123 EHEP from TNA inhibition. The inhibition experiments showed that the galactoside
124 hydrolytic activity of *aku*BGL decreased with increasing TNA concentration, indicating
125 that TNA inhibits *aku*BGL activity in a dose-dependent manner (Fig. 1A, Fig. S1A).
126 Approximately 70% *aku*BGL activity was inhibited at a TNA concentration of 40 μM.
127 Moreover, protection ability analysis revealed that EHEP protects *aku*BGL activity
128 from TNA inhibition in a dose-dependent manner, as indicated by the recovery of the
129 inhibited *aku*BGL activity with increasing EHEP concentration (Fig. 1B, Fig. S1B).
130 Further, approximately 80% of *aku*BGL activity was recovered at an EHEP
131 concentration of 3.36 μM.

132 Overall structure of EHEP

133 Considering the lack of known homologous proteins of EHEP, we determined the
134 structure of EHEP using the native-SAD method at a resolution of 1.15 Å, with a R_{work}
135 and R_{free} of 0.18 and 0.19, respectively (Table 1). The residues A21–V227 in purified
136 EHEP (1–20 aa were cleaved during maturation) were built, whereas two C-terminal
137 residues were disordered. The structure of EHEP consists of three PADs: PAD1 (N24–
138 C79), PAD2 (I92–C146), and PAD3 (F164–C221), which are linked by two long loops,
139 LL1 (Q80–N91) and LL2 (R147– G163), and arranged in a triangle shape (Fig. 2A).
140 These three PADs share a similar structure, with a root-mean-squared difference
141 (RMSD) of 1.065 Å over 46 Cα atoms and only ~20.3% sequence identity (Figs. 2B
142 and 2C). The three PADs share a canonical CBM14 fold consisting of two β-sheets

143 containing three N-terminal and two C-terminal antiparallel β-strands. Additionally,
144 two small α-helices were appended to the N- and C-terminus in PAD1 and PAD3 but
145 not in PAD2 (Fig. 2B).

146 Although the Dali server [15] did not provide similar structures using the overall
147 structure of EHEP as the search model, six structures showed similarities with a single
148 PAD of EHEP. These structures were the members of the PAD family, including the
149 chitin-binding domain of chitotriosidase (PDB ID 5HBF) [16], avirulence protein 4 from
150 *Pseudocercospora fuligena* [*Pf*Avr4 (PDB ID 4Z4A)] [17] and *Cladosporium fulvum*
151 [*Cf*Avr4 (PDBID 6BN0)] [18], allergen Der p 23 (PDB ID 4ZCE) [19], tachytitin (PDB ID
152 1DQC) [20], and allergen Blot 12 (PDB ID 2MFK), with Z-scores of 4.7–8.4, RMSD
153 values of 1.2–2.8 Å, and sequence identity of 19%–37%. The highest sequence
154 disparity was detected in PAD2, whereas the greatest structural differences were noted
155 in PAD3. The $C^{No1}X_{15}C^{No2}X_{5}C^{No3}X_{9}C^{No4}X_{12}C^{No5}X_{5\text{-}9}C^{No6}$ motif (superscripts and
156 subscripts indicate the cysteine number and number of residues between adjacent
157 cysteines, respectively) in each PAD of EHEP formed three disulfide bonds between
158 the following pairs: C^{No1}–C^{No3}, C^{No2}–C^{No6}, and C^{No4}–C^{No5} (Fig. 2B). Such rich disulfide
159 bonds may play a folding role in the structural formation of EHEP, with >70% of the
160 backbone in a loop conformation. A similar motif with disulfide bonds was observed in
161 tachycitin [20], *Pf*Avr4 [17], *Cf*Avr4 [18], and the chitin-binding domain of chitinase [16].
162 Although these proteins share a highly conserved core structure, they have different
163 biochemical characteristics. For example, the chitin-binding domain of human
164 chitotriosidase, Avr4 and tachycitin possess chitin-binding activity, but the critical
165 residues for chitin-binding are not conserved [16, 18, 21], indicating that they employ
166 different binding mechanisms. In contrast, EHEP and allergen Der p 23 do not possess
167 chitin-binding activity [4, 19]. Thus, the PAD family may participate in several
168 biochemical functions.

169 ## Modification of EHEP

170 Consistent with the molecular weight results obtained using MALDI–TOF MS [22],
171 the apo structure2 (1.4 Å resolution) clearly showed that the cleaved N-terminus of
172 Ala21 underwent acetylation (Fig. S2A), demonstrating that EHEP is acetylated in *A.*
173 *kurodai* digestive fluid. N-terminal acetylation is a common modification in eukaryotic
174 proteins. Such acetylation is associated with various biological functions, such as
175 protein half-life regulation, protein secretion, protein–protein interaction, protein–lipid
176 interaction [23], metabolism, and apoptosis [24]. Further, N-terminal acetylation may
177 stabilize proteins [25]. To explore whether acetylation affects the protective effects of
178 EHEP on *aku*BGL, we used the *E.coli* expression system to obtain the unmodified
179 recomEHEP (A21–K229). We measured the TNA-precipitating assay of recomEHEP.
180 The results revealed that recomEHEP precipitated after incubation with TNA, at a
181 comparable level to that of natural EHEP (Fig. S2B), indicating that acetylation is not
182 indispensable for the phlorotannin binding activity and stabilization of EHEP. Future
183 studies are warranted to verify the exact role of N-terminal acetylation of EHEP in
184 *A.kurodai*.

185 ## TNA binding to EHEP

186 To understand the mechanism by which TNA binds to EHEP, we determined the
187 structure of EHEP complexed with TNA (EHEP–TNA) using the soaking method. In
188 the obtained structure, both $2F_o–F_c$ and $F_o–F_c$ maps showed the electron density of
189 1,2,3,4,6-pentagalloylglucose, a core part of TNA missing the five external gallic acids
190 (Fig. 3A, Fig. S3A). Previous studies have shown that acid catalytic hydrolysis of TNA
191 requires a high temperature of 130°C [26]; even with a polystyrene-hollow sphere catalyst,
192 a temperature of 80°C is required [27]. Therefore, the five gallic acids could not be
193 visualized in the EHEP–TNA structure most likely due to the structural flexibility of
194 TNA.

195 The apo EHEP and EHEP–TNA structures were extremely similar, with an RMSD
196 value of 0.283 Å for 207 Cα atoms (Fig. S3B). However, the superposition of the two
197 structures showed a decrease of the loop part in EHEP–TNA. TNA binding caused a
198 slight increase in the α-helix and β-sheet contents of PAD2 and PAD3 (Fig. S3B). In
199 the EHEP–TNA structure, the residues C93–Y96 of PAD2 folded into an α-helix and
200 each β-sheet of the first β-strand in PAD3 elongated by incorporating one residue in the
201 first (G^{176}) and second β-sheets (S^{186}) and three residues in the third β-sheet ($H^{197}MP^{199}$).
202 The EHEP–TNA structure revealed that TNA binds to the center of the triangle
203 formed by the three PADs, a positively charged surface (Fig. 3A and Fig. S3C). The
204 binding pocket on EHEP surface was formed by the C-terminal α-helix of PAD1, the
205 N-terminal α-helix of PAD2, and the middle part (loop) of PAD3 assisted by two long
206 linker loops (LL1 and LL2). TNA was primarily bound to EHEP via hydrogen bonds
207 and hydrophobic interactions (Fig. 3B). Gallic acid1, 4, and 6 interacted with EHEP via
208 hydrogen bonds and additional hydrophobic contacts, whereas gallic acid2 and 3 only
209 interacted hydrophobically with EHEP. The 3-hydroxyl groups of gallic acid1 and 6
210 individually formed a hydrogen bond with the main chain of G74 and the side chain of
211 N75 in PAD1. The backbone carbonyl of Y96 and P199 in PAD2 and PAD3,
212 respectively, formed a hydrogen bond with the 3,5-hydroxyl groups of gallic acid4.
213 Additionally, some hydrogen bonds were formed between TNA and water molecules.
214 TNA binding was also stabilized by hydrophobic interactions between the benzene
215 rings of gallic acid and EHEP. For instance, gallic acid4 and 6 showed alkyl–π
216 interaction with P201 and P77, respectively; moreover, gallic acid3 and 4 formed
217 amide–π stackings with P199.
218 The EHEP–TNA structure clearly showed that TNA binds to EHEP without
219 covalent bonds and the binding does not induce significant structural changes; thus, we
220 attempted to recover EHEP from EHEP–TNA precipitates by adjusting the pH. As
221 hypothesized, re-solubilization of the EHEP–phlorotannin precipitate is pH-dependent
222 (Fig. 3C). The EHEP–TNA precipitate did not resolubilize at pH 7.0; however, after

223 incubating for >1 h at pH 7.5, the precipitate started resolubilizing. Most of the
224 precipitate rapidly resolubilized at an alkaline pH (≥8.0) after incubation for 15 min.
225 Further, the resolubilized EHEP had the same elution profile as that of the natural EHEP
226 (Fig. 3D) in SEC, suggesting that resolubilized EHEP maintained the native structure
227 and its phlorotannin-precipitate activity (Fig. S3D).

228 Two domains of *aku*BGL

229 To reveal the structural basis of *aku*BGL recognition of laminarin and inhibition
230 by TNA, we attempted to determine its structure. We soaked crystals in TNA as well as
231 various substrate solutions but finally obtained the optimal resolution using crystal
232 soaking in TNA. There was no electron density of TNA or something similar in the
233 2Fo–Fc and Fo–Fc map of the obtained structure; thus, we considered this structure as
234 the apo form of *aku*BGL.

235 Two *aku*BGL molecules were observed in an asymmetric unit (MolA and MolB).
236 These molecules lacked the N-terminal 25 residues (M1–D25), as confirmed using N-
237 terminal sequencing analysis of purified natural *aku*BGL. This N-terminal fragment
238 was predicted to be a signal peptide using the web server SignalP-5.0. The residues
239 L26–P978 were constructed in both MolA and MolB with glycosylation, whereas the
240 remaining C-terminal residues (A979–M994) could not be visualized as they were
241 disordered. The electron density map of Fo–Fc revealed N-glycosylation at three
242 residues, i.e., N113, N212, and N645 (Figs. S4A, B). N-glycosylation of GH enzymes
243 prevents proteolysis and increases thermal stability [28, 29]. Additionally, a study on β-
244 glucosidase *Aspergillus terreus* BGL demonstrated that N-glycosylation of N224
245 affected the folding stability, even when it is located close to a catalytic residue [30]. In
246 *aku*BGL, all N-glycosylation sites were present on the surface, far away from the
247 catalytic site. Therefore, we speculate that *aku*BGL glycosylation does not affect its
248 activity. Except for the difference in visualized glycans resulting from glycosylation,
249 MolA and MolB were similar, with a RMSD value of 0.182 for 899 Ca atoms; therefore,

250 we used MolA for further descriptions and calculations.

251 The structure of *aku*BGL consisted of two independent GH1 domains, GH1D1
252 (L26–T494) and GH1D2 (D513–P978), linked by a long loop (D495–Y512) (Fig. 4A).
253 There was little interaction between GH1D1 and GH1D2, only in a buried surface area
254 comprising 2% of the total surface (708.9 $Å^2$) (Fig. S4C). GH1D1 and GH1D2 have a
255 sequence identity of 40.47% and high structural similarity with an RMSD value of 0.59
256 Å for 371 Cα atoms (Fig. S5A upper panel).

257 Glucosidases of the GH1 family utilize the retaining mechanism with two glutamic
258 acids for catalyzing glucoside hydrolysis. In general, the distance between the two
259 catalytic oxygen atoms of the side chain of two glutamic acids is approximately 5 Å [31].
260 Sequence and structure alignment of GH1D1 and GH1D2 of *aku*BGL with other
261 members of the GH1 family revealed that the second glutamate is conserved (E404),
262 but the first glutamate is replaced by D192 in GH1D1. The oxygen atoms of the side
263 chains between D192 and E404 of GHD1 were 8.4 Å apart. In contrast, GH1D2
264 conserved two glutamic acids (E675 and E885) at the carboxyl termini of β-strands 4
265 and 7; the distance between oxygen atoms of E675 and E885 side chains was 5.1 Å
266 (Fig. S5A bottom panel), similar to that of *Neotermes koshunensis* BGL (*Nk*BGL, PDB
267 ID 3VIH) [32], *Nannochloropsis oceanica* BGL (*No*BGL, PDB ID 5YJ7) [33], and
268 *Spodoptera frugiperda* BGL (PDB ID 5CG0) (3.9–4.9Å) [34]. Furthermore, regarding the
269 two other conserved essential regions for β-glucosidase activity, namely, glycone-
270 binding site (GBS) and catalysis-related residues (CR), GH1D1 conserved neither GBS
271 nor CR, whereas GH1D2 conserved both (Fig. 4B). Altogether, we suggest that GH1D1
272 does not possess catalytic activity. We expressed and purified the recombinant GH1D1,
273 which did not show any hydrolytic activity toward O-PNG (Figs. S4D, E), although we
274 could not rule out the effect of N-glycosylation.

275 Structural comparison of GH1D2 with other BGLs, including *Nk*BGL (PDB ID
276 3VIH) [32], rice (*Oryza sativa L.)* BGL (*Os*BGL, PDB ID 2RGL) [35], and microalgae
277 *No*BGL (PDB ID 5YJ7) [33], revealed the characteristics of each active pocket (Fig. S5B).

278 *Os*BGL and *No*BGL have a deep, narrow, and straight pocket, whereas GH1D2 and
279 *Nk*BGL have a broad and crooked pocket. Such active pocket shapes reflect the
280 substrate preferences of *Os*BGL and *No*BGL; they hydrolyze laminaribiose with no
281 detectable activity toward laminaritetraose [33, 36]. Furthermore, the difference in the
282 features of large active pockets between *Nk*BGL and GH1D2, wherein GH1D2 often
283 possesses an auxiliary site with several aromatic residues bound to the carbohydrate via
284 CH–π interactions [37], may explain their substrate specificity. *Nk*BGL efficiently
285 hydrolyzes laminaribiose and cellobiose but has weak hydrolytic activity toward
286 laminarin [38]. In contrast, the GH1D2 of *aku*BGL has similar activity levels toward
287 cellobiose and laminarin [39]. Therefore, the GH1D2 of *aku*BGL may recognize larger
288 substrates than that of other BGLs. Laminarin typically has a curved conformation;
289 accordingly, narrow- and straight-shaped pockets are incompatible for binding.
290 Furthermore, we docked GH1D2 with laminaritetraose, wherein the four glucose units
291 formed extensive contacts with GH1D2. Hydrogen bonds involved the catalytic
292 residues E675. In addition, several aromatic residues, such as W631, F677, W681, F689,
293 Y819, Y846, W857, and W935, formed CH–π stacking (Fig. S6). Some interacting
294 residues belonged to GBS and CR sites, such as E675, W631, Y819, and W935.
295 Additionally, the docking structure revealed that the +3 and +4 glucose of
296 laminaritetraose is located at the auxiliary binding site and that atom O1 of the +4
297 glucose is positioned outside the pocket (Fig. S6), implying that the auxiliary binding
298 site with several aromatic residues (F677 and W681) of GH1D2 facilitates laminarin
299 binding.

300 Inhibitor binding of *aku*BGL

301 As we could not obtain the complex structure of *aku*BGL with TNA, we performed
302 docking calculations of *aku*BGL GH1D2 with TNA to explore the inhibition
303 mechanism. The docking model of *aku*BGL–TNA showed that seven gallic acid rings
304 of TNA formed an extensive hydrogen bond network with *aku*BGL in the binding

305 pocket (Fig. 5). The hydroxyl groups of TNA formed hydrogen bonds with the residues
306 N552, E675, D735, K739, K759, Q840, T844, D852, and K859 of GH1D2. Moreover,
307 benzene rings showed hydrophobic interactions with several hydrophobic residues. In
308 particular, stable π–π stacking was observed between TNA and residues F547, W631,
309 F689, Y846, W857, and W935. Among these residues, the conserved E675 was the
310 catalytic residue, and W631, W935, and E934 contributed to GBS and CR sites.

311 In addition, we performed a docking calculation of GH1D2 with the characteristic
312 inhibitors eckol and phloroglucinol [40]. The binding mechanisms of eckol and
313 phloroglucinol were similar to those of TNA but with different contact residues (Fig.
314 S7). For eckol, the six hydroxyl groups formed hydrogen bonds with residues E675,
315 D735, E737, K759, E885, and E934. Additionally, residues W631, F677, F689, Y819,
316 W857, W935, F943, and W927 formed π–π stacking with eckol. For phloroglucinol,
317 the three hydroxyl groups formed hydrogen bonds with E675, E885, and E934, whereas
318 residues W631, F689, Y819, W857, W935, and W927 formed π–π stacking with the
319 benzene ring.

320 The docking scores of the inhibitors TNA, eckol, and phloroglucinol were −8.8,
321 −7.3, and −5.7 kcal/mol, respectively, whereas the substrate laminaritetraose had a
322 docking score of −6.6 kcal/mol. Those docking scores corroborated well with the
323 inhibition activity toward *aku*BGL, that TNA had a more robust inhibition activity than
324 phloroglucinol [4], indicating that the docking results are reasonable. In summary, the
325 three inhibitors interacted with *aku*BGL through similar binding mechanisms to occupy
326 the substrate-binding site, suggesting a reversible competitive inhibition mechanism.

327 Discussion

328 In marine habitats, the ecological interactions between brown algae and herbivores
329 dominate marine ecosystems [41]. The *aku*BGL–phlorotannin/laminarin–EHEP system
330 represents the feeding defense–offense associations between *A. kurodai* and brown

331 algae. We focused on this system to understand the molecular mechanism at the atomic
332 level. In contrast to most GH1 BGLs containing one catalytic GH1 domain, *aku*BGL
333 consists of noncatalytic GH1D1 and catalytic GH1D2. The noncatalytic GH1D1 may
334 act as a chaperone of GH1D2, as we successfully overexpressed GH1D1 but failed to
335 do the same for GH1D2. Such multi-GH1D assembly and a similar function has been
336 suggested in β-glucosidase *Cj*CEL1A of *Corbicula japonica* [42] and glycosidase
337 *LpM*DGH1 of the shipworm *Lyrodus pedicellatus*[43]. *Cj*CEL1A has two tandem GH1Ds
338 with a sequence identity of 43.41% [42]. Two catalytic glutamic acids and the residues
339 related to substrate binding are conserved in the second GH1D, whereas the first GH1
340 domain lacks these conserved residues and may play a role in folding the catalytic
341 domain. *LpM*DGH1 consists of six GH1Ds, among which GH1D2, 4, 5, and 6 contain
342 the conserved residues for activity, whereas others do not contain these residues and
343 might be involved in protein folding or substrate interactions [43]. Future assay of GH1D2
344 and inactive mutants is the complement to validate the molecular mechanism of
345 *aku*BGL.

346 BGLs have different substrate preferences in the degree of polymerization and
347 type of glycosidic bond. In general, BGLs prefer to react with mono-oligo sugars over
348 polysaccharides. For instance, *Os*BGL, *No*BGL, and *Nk*BGL hydrolyze disaccharides
349 (cellobiose and laminaribiose) but display no or weak activity toward polysaccharides
350 (cellulose and laminarin) [33, 36, 38]. The structure of GH1D2 explained the substrate
351 preference for the polysaccharide laminarin. GH1D2 contains an additional auxiliary
352 site composed of aromatic residues (Fig. S5B) in the substrate entrance pocket, which
353 putatively enables it to accommodate a long substrate, contributing to *aku*BGL activity
354 toward laminarin, as supported by docking calculations (Fig. S6). In addition, docking
355 analysis of *aku*BGL GH1D2 with inhibitors (TNA, phlorotannin, eckol, and
356 phloroglucinol) revealed that these inhibitors bind to the substrate-binding site via
357 hydrogen bonds and hydrophobic interactions similar to laminarin. Such binding
358 mechanisms suggest the presence of competitive inhibition to occupy the binding site,

consistent with previous research [4]. Future kinetic experiments are required to validate quantitatively the competitive inhibition of phlorotannin against *aku*BGL.

EHEP, expressed in the midgut of *A. kurodai*, was identified as an antidefense protein, protecting the hydrolysis activity of *aku*BGL from phlorotannin inhibition [4]. Such an ecological balance also exists between plants and their predatory mammals and insects. Similar to brown algae, plants use the toxic secondary metabolite tannins as their defense mechanism against predators, which constitute 5%–10% of dry weight of leaves. In vertebrate herbivores, tannins reduce protein digestion [44]. In phytophagous insects, tannins may be oxidized at the alkaline pH of the insect midgut and cause damage to cells [45]. The evolution of plant–herbivore survival competition has led to the development of remarkably unique adaptation strategies. Mammals feeding on plants that contain tannin may overcome this defense by producing tannin-binding proteins, proline-rich proteins, and histatins [46] [47]. Proline constitutes at least 20% of the total amino acid content in proline-rich proteins; for some species, the proportion of proline reaches 40%. Histidine constitutes 25% of total amino acid content in histatins. Both proline-rich proteins and histatins are unfolding proteins with randomly coils in solution. In caterpillars, the oxidation damage of tannin is reduced by the low oxygen level. Some insects use the peritrophic membrane to transport tannins into the hemolymph, where they are excreted [48]. Additionally, the peritrophic envelop protects insects from tannins by forming an impermeable barrier to tannins [44]. *A. kurodai* uses a similar strategy to mammals by secreting the tannin-binding protein EHEP. Although EHEP has a completely different amino acid composition with proline-rich proteins and histatins, EHEP also binds to phlorotannin. Therefore, EHEP may be a specific counteradaptation that allows *A.kurodai* to feed on brown algae, as there are no homologous proteins in other organisms.

The three PADs of EHEP are arranged in a triangle shape, forming a large cavity on the surface at the triangle center to provide a ligand-binding site. EHEP has a positively charged surface at a pH of <6.0, whereas the surface becomes negatively charged at a

387 pH of >7.0 (Fig. S3C). Meanwhile, TNA has a pKa of 4.9–8 [49-51], showing minor
388 negative charges at an acidic pH and the highest negative charge at a pH of >7.0 [52].
389 Therefore, TNA binds to EHEP at a pH of <6.0 (pH of crystallization = 4.5), but it
390 shows charge repulsion with EHEP at a pH of >8.0. Altogether, TNA is protonated and
391 behaves as a hydrogen bond donor when the pH is below its pKa, whereas when the pH
392 is above its pKa, TNA is deprotonated and the hydrogen bonding cannot be maintained.
393 As losing hydrogen bonds and increasing repulsive forces at a pH >8.0, the precipitated
394 EHEP–TNA could dissolve in the buffer of pH >8.0. This pH-induced reversible
395 interaction also occurred in other proteins, such as BSA, pepsin, and cytochrome C [53].
396 The phlorotannin members share a similar structure with TNA; thus, we speculate that
397 the EHEP–phlorotannin complex also exhibits a pH-induced reversible interaction. *In*
398 *vivo*, the pH of the digestive fluid of *A. kurodai* is approximately 5.5[4], which favors the
399 binding of EHEP to phlorotannin. In the alkaline hindgut [54], the EHEP–phlorotannin
400 disassociates (Fig. 6), and the phlorotannin is subsequently excreted from the anus.
401 Based on the EHEP–TNA structure and docking models of *aku*BGL–
402 inhibitor/substrate, we proposed a mechanism of phlorotannin inhibition on *aku*BGL
403 activity and EHEP protection from phlorotannin inhibition (Fig. 6). Because laminarin
404 lacks the benzene rings essentially to form CH–π stacking interactions with EHEP, the
405 EHEP can be considered not binding with the laminarin. In the absence of EHEP,
406 phlorotannin occupies the substrate-binding site of *aku*BGL, inhibiting the substrate
407 from entering the active site and resulting in no glucose production. In the presence of
408 EHEP, it competitively binds to phlorotannin, freeing the *aku*BGL pocket. Then, the
409 substrate can enter the active pocket of *aku*BGL and glucose can be produced normally.
410 The digestive fluid of *A. kurodai* contains EHEP at a high concentration (>4.4 μM) [4],
411 which is slightly higher than the concentration of EHEP (3.36 μM) that protects
412 *aku*BGL activity (Fig. 1B). The high concentration of EHEP allows *A. kurodai* feeding
413 of phlorotannin-rich brown algae. The balance between phlorotannin inhibition and
414 protection is controlled by the concentrations of phlorotannin and EHEP *in vivo*.

415 The *aku*BGL–phlorotannin/laminarin–EHEP system is the digestive–defensive–
416 offensive associations between algae and herbivores. Our study presented the molecular
417 mechanism of this system at the atomic level, providing a molecular explanation for
418 how the sea hare *A. kurodai* utilizes EHEP to protect *aku*BGL activity from
419 phlorotannin inhibition. Further, such a feeding strategy has attracted attention for
420 producing glucose as a renewable biofuel source, so our studies provide a molecular
421 basis for the biofuel industry applications of brown algae.

422 Materials and Methods

423 EHEP and *aku*BGL preparation

424 Natural EHEP (22.5 kDa) and *aku*BGL (110 kDa) were purified from *A. kurodai*
425 digestive fluid as described previously [4]. For crystallization, we further added one step
426 for purification of EHEP using size exclusion chromatography (HiLoad 16/60 Superdex
427 75, GE Healthcare), for which the column was equilibrated with 20 mM MES-NaOH
428 buffer (pH 6.5). Obtained EHEP was then concentrated to 15–25 mg/mL using
429 Vivaspin-4 10K columns (Sartorius, Göttingen, Germany). About *aku*BGL, we
430 exchanged buffer from 20 mM Tris-HCl pH 7.0 to 20 mM Bis-tris pH 6.0 and
431 concentrated it to 11 mg/mL using Amicon with a cutoff of 50 kDa.
432 To verify whether the chemical modification which was indicated by previous
433 study[22] affects the function of EHEP, we prepared recombinant EHEP (recomEHEP)
434 without the N-terminal signal peptide (1–20 aa) and chemical modifications [22]. EHEP
435 cDNA was obtained via reverse transcription–polymerase chain reaction (RT–PCR)
436 using the total RNA of *A. kurodai* as a template. The reamplified fragment was digested
437 and ligated to a plasmid derived from pET28a (Novagene, Darmstadt, Germany). We
438 transformed the plasmid containing recomEHEP into *E. coli* B834(DE3) pARE2 and
439 expressed it with a C-terminal hexahistidine-tag. The cells were cultured in lysogeny

440 broth (LB) medium with the antibiotics kanamycin (25 mg/L) and chloramphenicol (34
441 mg/L) until the optical density at 600 nm (OD_{600}) reached 0.6. Subsequently,
442 overexpression was induced by adding 0.5 mM isopropyl b-D-L-thiogalactopyranoside
443 for 20 h at 20 °C. After harvesting by centrifugation, the cells were resuspended in a
444 buffer containing 50 mM Tris-HCl pH 7.4, 300 mM NaCl, DNase, and lysozyme and
445 were disrupted via sonication. The insoluble part was removed by centrifugation for 30
446 min at 40000 ×*g* at 4 °C. We loaded the supernatant onto a 5-mL Histrap HP column
447 and the recomEHEP was eluted using increasing concentrations of imidazole (0–500
448 mM). The purified proteins were dialyzed against a solution containing 50 mM Tris-
449 HCl pH 7.4 and 50 mM NaCl and subsequently loaded onto a Hitrap Q column and
450 eluted by a linear gradient of a solution containing 50 mM Tris-HCl and 1 M NaCl.
451 Fractions containing recomEHEP were concentrated and then purified using a gel
452 filtration column (Hiload 16/60 superdex 75 pg) equilibrated with 20 mM sodium
453 acetate pH 6.0 and 100 mM NaCl. We collected the fractions containing recomEHEP
454 and concentrated them to 2.1 mg/mL using Amicon (Merck, American).

455 DNA encoding *aku*BGL without signal peptide was codon optimized (GENEWIZ,
456 China) for overexpress in *E. coli*, and cDNA encoding GH1D1 domain was subcloned
457 to a modified pET-32a vector (Invitrogen, USA) with an N-terminal TrxA tag and a
458 6×His tag followed by a TEV protease recognition site. The plasmid pET-32a-GH1D1
459 was electorally transformed into *E.coli* origami2 cells. We grew the cells in LB medium
460 supplemented with 100 μg/mL of ampicillin at 37 °C until the OD_{600} reached 0.6. Then
461 the cultures were cooled and induced with 0.5 mM isopropyl-β-D-
462 thiogalactopyranoside at 20 °C for 16 h. After resuspending the harvested cells in a
463 buffer containing 50 mM Tris-HCl (pH 7.4), 250 mM NaCl, and 5% glycerol, we
464 disrupted the cells by sonication. The cell lysate was centrifugated at 40,000 ×g for 30
465 min at 4 °C. The supernatant was filtered by 0.45 μm membrane and then loaded onto
466 a Histrap HP column (GE, USA). After washing with lysis buffer supplemented with
467 20 mM imidazole, the recomGH1D1 was eluted linearly from the column with lysis

468 buffer supplemented with 500 mM imidazole. The fractions containing recomGH1D1
469 were added with TEV protease at a ratio of 1:10 and dialyzed against the buffer
470 containing 50 mM Tris (pH 7.4), 50 mM NaCl, and 2 mM DTT at 4 °C overnight. Then,
471 we purified the recomGH1D1 by a Histrap HP column again, and collected the
472 flowthrough. Finally, we purified the recomGH1D1 by size exclusion chromatography
473 on a Hiload 16/60 200 pg column (GE, USA) equilibrated with a buffer containing 20
474 mM Bis-Tris (pH 6.0). The recomGH1D1 was concentrated to 1.5 mg/mL by
475 centrifugation using Amicon Ultra with 10 kDa. cutoff.

476 N-terminal sequencing of *aku*BGL

477 We performed a N-terminal sequencing of purified *aku*BGL using the Edman
478 degradation method. *aku*BGL was separated by SDS–PAGE, followed by
479 electrophoretic transfer onto a PVDF (polyvinylidene fluoride) membrane (GE,
480 American). The membrane was subsequently stained with Ponceau S solution. The
481 band corresponding to *aku*BGL was excised and analyzed using a PPSQ-53A Protein
482 sequencer (Shimadzu, Japan) at the Instrumental Analysis Service of Hokkaido
483 University.

484 Effects of TNA on *aku*BGL activity with or without EHEP

485 Due to the yellow color of TNA, which affects absorbance at 420 nm of the
486 reaction product o-nitrophenol of *aku*BGL, we used HPLC to measure the *aku*BGL
487 activity in the reaction system involving TNA. Ortho-nitrophenyl-β-galactoside
488 (ONPG) was used as a substrate to measure *aku*BGL activity. The reaction system (100
489 μL) included 2.5 mM ONPG, 49 nM *aku*BGL, and different TNA concentrations in a
490 reaction buffer (50 mM CH_3COONa pH 5.5, 100 mM NaCl, and 10 mM $CaCl_2$). After
491 incubation for 10 min at 37 °C, 100 μL of methanol was added to each sample to
492 terminate the reaction. Then, the mixture was centrifuged for 10 min at 15000 ×*g* at 4 °C

493 and the supernatant was used for analyzing *aku*BGL activity via HPLC. To measure the
494 protective effect of EHEP on *aku*BGL, we added different amounts of EHEP to the
495 reaction system.

496 RecomGH1D1 activity assay

497 We measured simply the activity of the recomGH1D1 using a spectrophotometer
498 because the reaction product o-nitrophenol is yellow. The reaction system (100 μL)
499 included 2.5 mM ONPG, 49 nM *aku*BGL or recomGH1D1 in a reaction buffer (50 mM
500 CH_3COONa pH 5.5, 100 mM NaCl, and 10 mM $CaCl_2$). After incubation for 10 min at
501 37 °C, the reaction was terminated by adding 100 μL of 500 mM Na_2CO_3. The
502 absorbance at 420 nm was measured using a SpectraMax spectrophotometer
503 (Molecular Devices, Japan).

504 Binding assay for recomEHEP with TNA

505 We measured the binding activity of recomEHEP using precipitation analysis in
506 same method of natural EHEP, as described previously [4]. Briefly, recomEHEP or EHEP
507 was incubated with TNA at 25 °C for 90 min and centrifuged for 10 min at 12000 ×*g* at
508 4 °C. Then, we washed the precipitates twice and resuspended them in an SDS–PAGE
509 loading buffer for binding analysis.

510 Resolubilization of the EHEP–eckol precipitate

511 A mixture of 2 mg of EHEP and 0.4 mg of eckol was incubated at 37 °C for 1 h,
512 followed by centrifugation at 12000 ×g for 10 min, and the supernatant was removed.
513 The sediment was dissolved in 50 mM Tris-HCl buffer at different pH (7.0–9.0) and
514 the absorbance at 560 nm was measured over time. After checking the elution peak by
515 SDS–PAGE, the resolubilized EHEP was analyzed by a Sephacryl S-100 HR column
516 (2.0 ×110 cm). Moreover, the eckol/dieckol-binding activity of resolubilized EHEP was

517 assessed, as mentioned above in this section.

518 Crystallization and data collection

519 The crystallization, data collection, and initial phase determination of EHEP were
520 described previously [22]. As EHEP precipitates when bound to TNA, we could not
521 cocrystallize EHEP with TNA. Therefore, we used the soaking method to obtain the
522 EHEP–TNA complex. Owing to the poor reproducibility of EHEP crystallization, we
523 used a co-cage-1 nucleant [55] to prepare EHEP crystals for forming the complex with
524 TNA. Finally, we obtained high-quality EHEP crystals under the reservoir solution
525 containing 1.0 M sodium acetate, 0.1 M imidazole (pH 6.5) with co-cage-1 nucleant.
526 Subsequently, we soaked the EHEP crystals in a reservoir solution containing 10 mM
527 TNA at 37 °C for 2 days; then, they were maintained at 20 °C for 2 weeks. Next, we
528 soaked the EHEP crystals in a reservoir solution containing 10 mM phloroglucinol. For
529 data collection, the crystal was soaked in a cryoprotectant solution containing 20% (v/v)
530 glycerol along with the reservoir solution. Diffraction data were collected under a cold
531 nitrogen gas stream at 100 K using Photon Factory BL-17 (Tsukuba, Japan) or Spring
532 8 BL-41XU (Hyogo, Japan).

533 For *aku*BGL crystallization, the initial crystallization screening was performed
534 using the sitting-drop vapor-diffusion method with Screen classics and Classics II
535 crystallization kits (Qiagen, Hilden, Germany) and PACT kits (Molecular Dimensions,
536 Anatrace, Inc.) at 20 °C. Crystallization drops were set up by mixing 0.5 μL of protein
537 solution with an equal volume of the reservoir solution. The initial crystals were
538 obtained under condition no. 41 (0.1 M sodium acetate pH 4.5 and 25% polyethylene
539 glycol [PEG] 3350) of Classics II, no. 13 (0.1 M MIB buffer [25 mM sodium malonate
540 dibasic monohydrate, 37.5 mM imidazole, and 37.5 mM boric acid], with pH 4.0 and
541 25% PEG 1500), and no. 37 (0.1 M MMT buffer [20 mM DL-malic acid, 40 mM MES
542 monohydrate, and 40 mM Tris], with pH 4.0 and 25% PEG 1500) of PACT. After
543 optimization by varying the buffer pH and precipitant concentration and adding co-

544 cage1 nucleant, the optimal crystals were obtained using 0.1 M sodium acetate pH 4.5,
545 and 20% PEG 3350 with a co-cage1 nucleant at a protein concentration of 5.4 mg/mL.
546 Diffraction data were collected under a cold nitrogen gas stream at 100 K using Photon
547 Factory BL-1A (Tsukuba, Japan) after cryoprotection by adding glycerol to a 20% final
548 concentration into the reservoir solution. The optimal resolution of diffraction data was
549 obtained by soaking a crystal with 5 mM TNA in the reservoir buffer at 37 °C for 4 h.
550 All datasets were indexed, integrated, scaled, and merged using *XDS/XSCALE*
551 program [56]. Statistical data collection and process are summarized in Table 1.

552 Structure determination and refinement

553 For EHEP structure determination, after initial phasing via the native-SAD
554 method[22, 57], the model was obtained and refined with *auto-building* using
555 *Phenix.autobuild* of *Phenix* software suite [58]. The obtained native-SAD structure was
556 used as a model for rigid body refinement using *phenix.refine* [59] of *Phenix* software
557 suite with a native data at high resolution of 1.15 Å. The structure of EHEP was
558 automatically rebuilt using *Phenix.autobuild* of the *Phenix* software suite again [58].
559 Several rounds of refinement were performed using *Phenix.refine* of the *Phenix*
560 software suite [58], alternating with manual fitting and rebuilding using *COOT* program
561 [60]. The final refinement statistics and geometry are shown in Table 1.
562 The structure of the EHEP–TNA complex was determined via the molecular
563 replacement (MR) method using the EHEP structure as a search model with *Phaser*
564 of *Phenix* software suite [61]. The electron density block of TNA was clearly shown in
565 both $2F_o$–F_c and F_o–F_c maps. Subsequently, TNA structure was manually constructed,
566 followed by several rounds of refinement using *Phenix.refine* [58], with manual fitting
567 and rebuilding using *COOT* [60]. We also determined the structure of phloroglucinol-
568 soaked crystals at a resolution of 1.4 Å via the MR method using the refined EHEP
569 structure as a search model with *Phaser*, but no electron density block of phloroglucinol
570 was obtained. Therefore, we referred to this structure as the apo form (apo structure2).

571 The final refinement statistics and geometry are shown in Table 1.

572 We determined the structure of *aku*BGL via the MR method using *Phaser* of
573 *Phenix* software suite [61]. We used one GH domain (86–505 aa) of β-klotho (PDB entry:
574 5VAN) [62] as the search model. This GH domain of β-klotho shares 30% sequence
575 identity with *aku*BGL. Four GH domains of two molecules in an asymmetric unit were
576 found and subsequently rebuilt with *Phenix_autobuild* of *Phenix* software suite [58].
577 Finally, refinement of *aku*BGL structure was performed as described for EHEP.

578 Docking studies of *aku*BGL with phlorotanins and laminarins

579 We used Schrodinger Maestro program for performing docking studies [63]. First,
580 we superimposed the structure of *Os*BGL mutant complexed with cellotetraose (PDB
581 ID 4QLK [64]) to that of *aku*BGL GH1D2 to define the ligand position in the ligand-
582 binding cavity. Then, we modified the structure of the *aku*BGL GH1D2 using wizard
583 module to remove water molecules and add hydrogen atoms for docking. The 2D
584 structures of the inhibition ligands, including TNA, phloroglucinol, and eckol, were
585 downloaded from Pubchem [65] and further converted to 3D structures using the LigPrep
586 module of Schrodinger Maestro program. The structure of the substate laminaritetraose
587 was extracted from the *Zobellia galactanivorans* *β*-glucanase–laminaritetraose
588 complex structure (PDB ID: 4BOW) [66]. Then, a receptor grid was constructed in the
589 center of the ligand-binding cavity. We performed docking using the Glide standard
590 precision mode without any constraints. The optimal binding pose was determined
591 using the lowest Glide score, and docked structures were analyzed using PyMol.

592 Data Availability

593 The atomic coordinates were deposited in the PDB with the accession codes as
594 follows: EHEP with 1.15 Å resolution (8IN3), EHEP with 1.4 Å resolution (8IN4),
595 EHEP complexed with tannic acid (8IN6), *aku*BGL(8IN1).

596

597 # Acknowledgments

598 This work was supported in part by Grant-in-Aid for Scientific Research (B)
599 (Grant Number 21H01754 To M. Y) and Platform Project for Supporting Drug
600 Discovery and Life Science Research (Basis for Supporting Innovative Drug Discovery
601 and Life Science Research (BINDS)) from Japan Agency for Medical Research and
602 Development (AMED) under Grant Number JP18am0101071 and JP19am0101083.
603 We are grateful to the Photon Factor and SPring-8 (No. 2017B2545, 2017A2551,
604 2018B2538) for beam time and the beamline staff for their assistance for data collection.

605

606 # References

607 1. Becklin, K.M. A Coevolutionary Arms Race: Understanding Plant-Herbivore
608 Interactions. *The American Biology Teacher* **70**, 288-292 (2008).
609 2. Jormalainen, V. & Honkanen, T. in Algal Chemical Ecology 57-89 (2008).
610 3. Enquist-Newman, M. et al. Efficient ethanol production from brown
611 macroalgae sugars by a synthetic yeast platform. *Nature* **505**, 239-243 (2014).
612 4. Tsuji, A., Kuwamura, S., Shirai, A. & Yuasa, K. Identification and
613 Characterization of a 25 kDa Protein That Is Indispensable for the Efficient
614 Saccharification of Eisenia bicyclis in the Digestive Fluid of Aplysia kurodai.
615 *PLoS One* **12**, e0170669 (2017).

616 5. Erb, M. & Reymond, P. Molecular Interactions Between Plants and Insect
617 Herbivores. *Annu Rev Plant Biol* **70**, 527-557 (2019).
618 6. Mendez-Liter, J.A., de Eugenio, L.I., Prieto, A. & Martinez, M.J. The beta-
619 glucosidase secreted by Talaromyces amestolkiae under carbon starvation: a
620 versatile catalyst for biofuel production from plant and algal biomass.
621 *Biotechnol Biofuels* **11**, 123 (2018).
622 7. Nakajima, M., Yamashita, T., Takahashi, M., Nakano, Y. & Takeda, T.
623 Identification, cloning, and characterization of beta-glucosidase from Ustilago
624 esculenta. *Appl Microbiol Biotechnol* **93**, 1989-1998 (2012).
625 8. Wang, Z. et al. A novel Vibrio beta-glucosidase (LamN) that hydrolyzes the
626 algal storage polysaccharide laminarin. *FEMS Microbiol Ecol* **91**, fiv087 (2015).
627 9. Kim, D.H., Kim, D.H., Lee, S.H. & Kim, K.H. A novel beta-glucosidase from
628 Saccharophagus degradans 2-40(T) for the efficient hydrolysis of laminarin
629 from brown macroalgae. *Biotechnol Biofuels* **11**, 64 (2018).
630 10. Mohsin, I., Poudel, N., Li, D.C. & Papageorgiou, A.C. Crystal Structure of a
631 GH3 beta-Glucosidase from the Thermophilic Fungus Chaetomium
632 thermophilum. *Int J Mol Sci* **20** (2019).
633 11. Hegedus, D., Erlandson, M., Gillott, C. & Toprak, U. New Insights into
634 Peritrophic Matrix Synthesis, Architecture, and Function. *Annual Review of*
635 *Entomology* **54**, 285-302 (2009).
636 12. Devenport, M. et al. Identification of the Aedes aegypti peritrophic matrix

637 protein AeIMUCI as a heme-binding protein. *Biochemistry* **45**, 9540-9549
638 (2006).
639 13. Cassani, L. et al. Seaweed-based natural ingredients: Stability of phlorotannins
640 during extraction, storage, passage through the gastrointestinal tract and
641 potential incorporation into functional foods. *Food Res Int* **137**, 109676 (2020).
642 14. Imbs, T.I. & Zvyagintseva, T.N. Phlorotannins are Polyphenolic Metabolites of
643 Brown Algae. *Russian Journal of Marine Biology* **44**, 263-273 (2018).
644 15. Holm, L. & Rosenstrom, P. Dali server: conservation mapping in 3D. *Nucleic*
645 *Acids Res* **38**, W545-549 (2010).
646 16. Fadel, F. et al. X-Ray Crystal Structure of the Full Length Human
647 Chitotriosidase (CHIT1) Reveals Features of Its Chitin Binding Domain. *PLoS*
648 *One* **11**, e0154190 (2016).
649 17. Kohler, A.C. et al. Structural Analysis of an Avr4 Effector Ortholog Offers
650 Insight into Chitin Binding and Recognition by the Cf-4 Receptor. *Plant Cell*
651 **28**, 1945-1965 (2016).
652 18. Hurlburt, N.K., Chen, L.H., Stergiopoulos, I. & Fisher, A.J. Structure of the
653 Cladosporium fulvum Avr4 effector in complex with (GlcNAc)6 reveals the
654 ligand-binding mechanism and uncouples its intrinsic function from recognition
655 by the Cf-4 resistance protein. *PLoS Pathog* **14**, e1007263 (2018).
656 19. Mueller, G.A. et al. Serological, genomic and structural analyses of the major
657 mite allergen Der p 23. *Clin Exp Allergy* **46**, 365-376 (2016).

658 20. Suetake, T. et al. Chitin-binding proteins in invertebrates and plants comprise a
659 common chitin-binding structural motif. *J Biol Chem* **275**, 17929-17932 (2000).
660 21. Madland, E., Crasson, O., Vandevenne, M., Sorlie, M. & Aachmann, F.L. NMR
661 and Fluorescence Spectroscopies Reveal the Preorganized Binding Site in
662 Family 14 Carbohydrate-Binding Module from Human Chitotriosidase. *ACS*
663 *Omega* **4**, 21975-21984 (2019).
664 22. Sun, X. et al. Crystallographic analysis of Eisenia hydrolysis-enhancing protein
665 using a long wavelength for native-SAD phasing. *Acta Crystallographica*
666 *Section F-Structural Biology Communications* **76**, 20-24 (2020).
667 23. Silva, R.D. & Martinho, R.G. Developmental roles of protein N-terminal
668 acetylation. *Proteomics* **15**, 2402-2409 (2015).
669 24. Hollebeke, J., Van Damme, P. & Gevaert, K. N-terminal acetylation and other
670 functions of Nalpha-acetyltransferases. *Biol Chem* **393**, 291-298 (2012).
671 25. Lange, P.F. & Overall, C.M. TopFIND, a knowledgebase linking protein termini
672 with function. *Nat Methods* **8**, 703-704 (2011).
673 26. Jie Fu, J.x., Zhang, Y. & Lu, X. A Greener Process for Gallic Acid Production
674 from Tannic Acid Hydrolysis with Hydrochloric Acid. *Asian Journal of*
675 *Chemistry* **27**, 3328-3332 (2015).
676 27. Luo, Q. et al. A novel green process for tannic acid hydrolysis using an
677 internally sulfonated hollow polystyrene sphere as catalyst. *RSC Advances* **8**,
678 17151-17158 (2018).

679 28. Amore, A. et al. Distinct roles of N- and O-glycans in cellulase activity and
680 stability. *Proc Natl Acad Sci U S A* **114**, 13667-13672 (2017).
681 29. Han, C. et al. Improvement of the catalytic activity and thermostability of a
682 hyperthermostable endoglucanase by optimizing N-glycosylation sites.
683 *Biotechnol Biofuels* **13**, 30 (2020).
684 30. Wei, W. et al. N-glycosylation affects the proper folding, enzymatic
685 characteristics and production of a fungal beta-glucosidas. *Biotechnol Bioeng*
686 **110**, 3075-3084 (2013).
687 31. Hayashi, Y. et al. Klotho-related protein is a novel cytosolic neutral beta-
688 glycosylceramidase. *J Biol Chem* **282**, 30889-30900 (2007).
689 32. Jeng, W.Y. et al. High-resolution structures of Neotermes koshunensis beta-
690 glucosidase mutants provide insights into the catalytic mechanism and the
691 synthesis of glucoconjugates. *Acta Crystallogr D Biol Crystallogr* **68**, 829-838
692 (2012).
693 33. Dong, S. et al. Structural insight into a GH1 beta-glucosidase from the
694 oleaginous microalga, Nannochloropsis oceanica. *Int J Biol Macromol* **170**,
695 196-206 (2021).
696 34. Tamaki, F.K. et al. Using the Amino Acid Network to Modulate the Hydrolytic
697 Activity of beta-Glycosidases. *PLoS One* **11**, e0167978 (2016).
698 35. Chuenchor, W. et al. Structural insights into rice BGlu1 beta-glucosidase
699 oligosaccharide hydrolysis and transglycosylation. *J Mol Biol* **377**, 1200-1215

700 (2008).

701 36. Opassiri, R. et al. Characterization of a rice β-glucosidase highly expressed in
702 flower and germinating shoot. *Plant Science* **165**, 627-638 (2003).

703 37. Hudson, K.L. et al. Carbohydrate-Aromatic Interactions in Proteins. *J Am Chem*
704 *Soc* **137**, 15152-15160 (2015).

705 38. Ni, J., Tokuda, G., Takehara, M. & Watanabe, H. Heterologous expression and
706 enzymatic characterization of .BETA.-glucosidase from the drywood-eating
707 termite, Neotermes koshunensis. *Applied Entomology and Zoology* **42**, 457-463
708 (2007).

709 39. Tsuji, A., Tominaga, K., Nishiyama, N. & Yuasa, K. Comprehensive enzymatic
710 analysis of the cellulolytic system in digestive fluid of the Sea Hare Aplysia
711 kurodai. Efficient glucose release from sea lettuce by synergistic action of 45
712 kDa endoglucanase and 210 kDa ss-glucosidase. *PLoS One* **8**, e65418 (2013).

713 40. Jung, H.A., Oh, S.H. & Choi, J.S. Molecular docking studies of phlorotannins
714 from Eisenia bicyclis with BACE1 inhibitory activity. *Bioorg Med Chem Lett*
715 **20**, 3211-3215 (2010).

716 41. Amsler, C.D. & Fairhead, V.A. in Advances in Botanical Research, Vol 43:
717 Incorporating Advances in Plant Pathology, Vol. 43. (ed. J.A. Callow) 1-91
718 (2006).

719 42. Sakamoto, K., Uji, S., Kurokawa, T. & Toyohara, H. Molecular cloning of
720 endogenous beta-glucosidase from common Japanese brackish water clam

721 Corbicula japonica. *Gene* **435**, 72-79 (2009).

722 43. Sabbadin, F. et al. Uncovering the molecular mechanisms of lignocellulose
723 digestion in shipworms. *Biotechnol Biofuels* **11**, 59 (2018).

724 44. Barbehenn, R.V. & Peter Constabel, C. Tannins in plant-herbivore interactions.
725 *Phytochemistry* **72**, 1551-1565 (2011).

726 45. Marsh, K.J. et al. New approaches to tannin analysis of leaves can be used to
727 explain in vitro biological activities associated with herbivore defence. *New*
728 *Phytol* **225**, 488-498 (2020).

729 46. Shimada, T. Salivary proteins as a defense against dietary tannins. *J Chem Ecol*
730 **32**, 1149-1163 (2006).

731 47. De Smet, K. & Contreras, R. Human Antimicrobial Peptides: Defensins,
732 Cathelicidins and Histatins. *Biotechnology Letters* **27**, 1337-1347 (2005).

733 48. War, A.R. et al. in Co-Evolution of Secondary Metabolites 795-822 (2020).

734 49. Lin, D. et al. The effect of ionic strength and pH on the stability of tannic acid-
735 facilitated carbon nanotube suspensions. *Carbon* **47**, 2875-2882 (2009).

736 50. Ge, D., Yuan, H., Shen, Y., Zhang, W. & Zhu, N. Improved sludge
737 dewaterability by tannic acid conditioning: Temperature, thermodynamics and
738 mechanism studies. *Chemosphere* **230**, 14-23 (2019).

739 51. Yi, Z. et al. Green, effective chemical route for the synthesis of silver nanoplates
740 in tannic acid aqueous solution. *Colloids and Surfaces A: Physicochemical and*
741 *Engineering Aspects* **392**, 131-136 (2011).

742 52. Dultz, S., Mikutta, R., Kara, S.N.M., Woche, S.K. & Guggenberger, G. Effects
743 of solution chemistry on conformation of self-aggregated tannic acid revealed
744 by laser light scattering. *Sci Total Environ* **754**, 142119 (2021).
745 53. Han, Y. et al. Polyphenol-Mediated Assembly of Proteins for Engineering
746 Functional Materials. *Angew Chem Int Ed Engl* **59**, 15618-15625 (2020).
747 54. Lemke, T., Stingl, U., Egert, M., Friedrich, M.W. & Brune, A. Physicochemical
748 conditions and microbial activities in the highly alkaline gut of the humus-
749 feeding larva of Pachnoda ephippiata (Coleoptera: Scarabaeidae). *Appl Environ*
750 *Microbiol* **69**, 6650-6658 (2003).
751 55. Yao, M. & Li, L. (NATIONAL UNIVERSITY CORPORATION
752 HOKKAIDO UNIVERSITY 2022).
753 56. Kabsch, W. Xds. *Acta Crystallogr D Biol Crystallogr* **66**, 125-132 (2010).
754 57. Yu, J., Shinoda, A., Kato, K., Tanaka, I. & Yao, M. A solution-free crystal-
755 mounting platform for native SAD. *Acta Crystallogr D Struct Biol* **76**, 938-945
756 (2020).
757 58. Adams, P.D. et al. PHENIX: a comprehensive Python-based system for
758 macromolecular structure solution. *Acta Crystallogr D Biol Crystallogr* **66**,
759 213-221 (2010).
760 59. Afonine, P.V. et al. Towards automated crystallographic structure refinement
761 with phenix.refine. *Acta Crystallogr D Biol Crystallogr* **68**, 352-367 (2012).
762 60. Emsley, P. & Cowtan, K. Coot: model-building tools for molecular graphics.

763 *Acta Crystallogr D Biol Crystallogr* **60**, 2126-2132 (2004).

764 61. McCoy, A.J. et al. Phaser crystallographic software. *J Appl Crystallogr* **40**, 658-
765 674 (2007).

766 62. Lee, S. et al. Structures of beta-klotho reveal a 'zip code'-like mechanism for
767 endocrine FGF signalling. *Nature* **553**, 501-505 (2018).

768 63. Sastry, G.M., Adzhigirey, M., Day, T., Annabhimoju, R. & Sherman, W. Protein
769 and ligand preparation: parameters, protocols, and influence on virtual
770 screening enrichments. *Journal of Computer-Aided Molecular Design* **27**, 221-
771 234 (2013).

772 64. Pengthaisong, S. & Ketudat Cairns, J.R. Effects of active site cleft residues on
773 oligosaccharide binding, hydrolysis, and glycosynthase activities of rice BGlu1
774 and its mutants. *Protein Sci* **23**, 1738-1752 (2014).

775 65. Wang, Y.L. et al. PubChem: a public information system for analyzing
776 bioactivities of small molecules. *Nucleic Acids Research* **37**, W623-W633
777 (2009).

778 66. Labourel, A. et al. The beta-glucanase ZgLamA from Zobellia galactanivorans
779 evolved a bent active site adapted for efficient degradation of algal laminarin. *J*
780 *Biol Chem* **289**, 2027-2042 (2014).

781 67. Hakulinen, N., Paavilainen, S., Korpela, T. & Rouvinen, J. The crystal structure
782 of beta-glucosidase from Bacillus circulans sp. alkalophilus: ability to form long
783 polymeric assemblies. *J Struct Biol* **129**, 69-79 (2000).

785 Fig 1

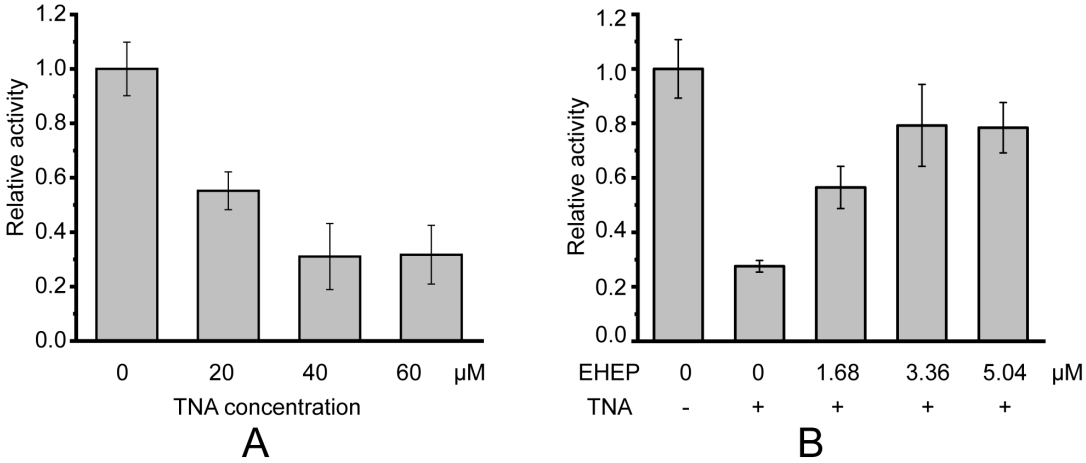

786

787 **Figure 1.** Galactoside hydrolytic activity of *aku*BGL toward ortho-Nitrophenyl-β-
788 galactoside. Activity (%) is shown as the fold increase relative to *aku*BGL without the
789 addition of TNA nor EHEP. (A) The hydrolytic activity of *aku*BGL (0.049 μM) with
790 TNA at different concentrations. (B) The hydrolytic activity of *aku*BGL (0.049 μM)
791 with 40 μM TNA and EHEP at different concentrations. The average and standard
792 deviation of the relative activity were estimated from three independent replicates (N =
793 3).

794 Fig 2

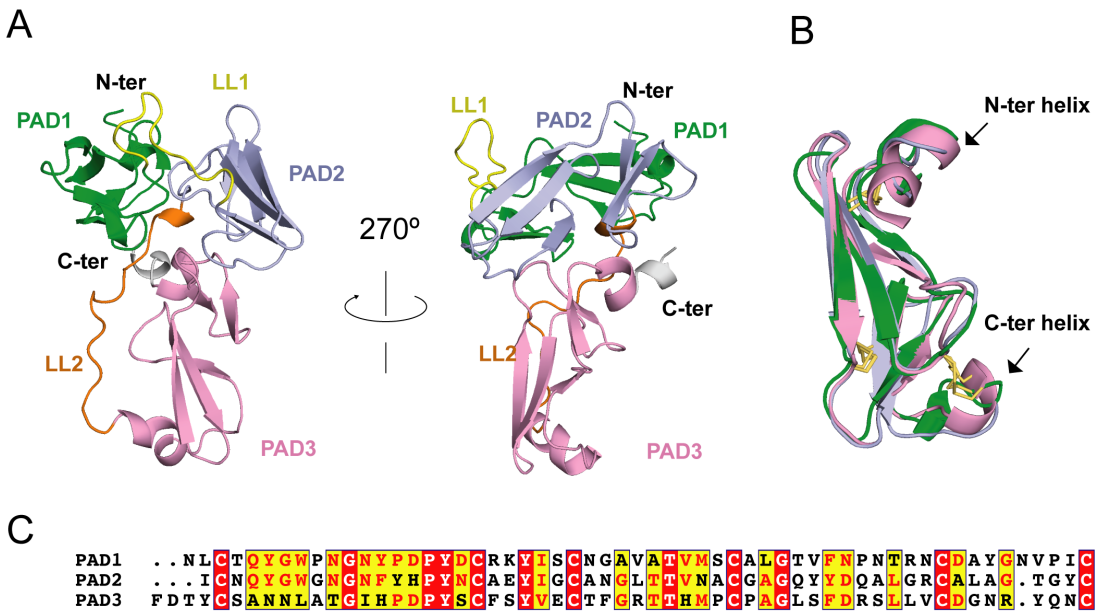

795

796 **Figure 2.** EHEP structure. (A) Cartoon representation of EHEP. The three PAD
797 domains are colored green, light blue, and pink, respectively. Linker long loop1 (LL1)
798 and loop2 (LL2) are colored yellow and blue. (B) Structural superposition of the three
799 PAD domains of EHEP. The three domains are colored as in (A). The disulfide bonds
800 are shown as yellow sticks. (C) Sequence alignment of three PAD domains. Alignment
801 was performed by CLUSTALW and displayed with ESPript3.

802 Fig 3

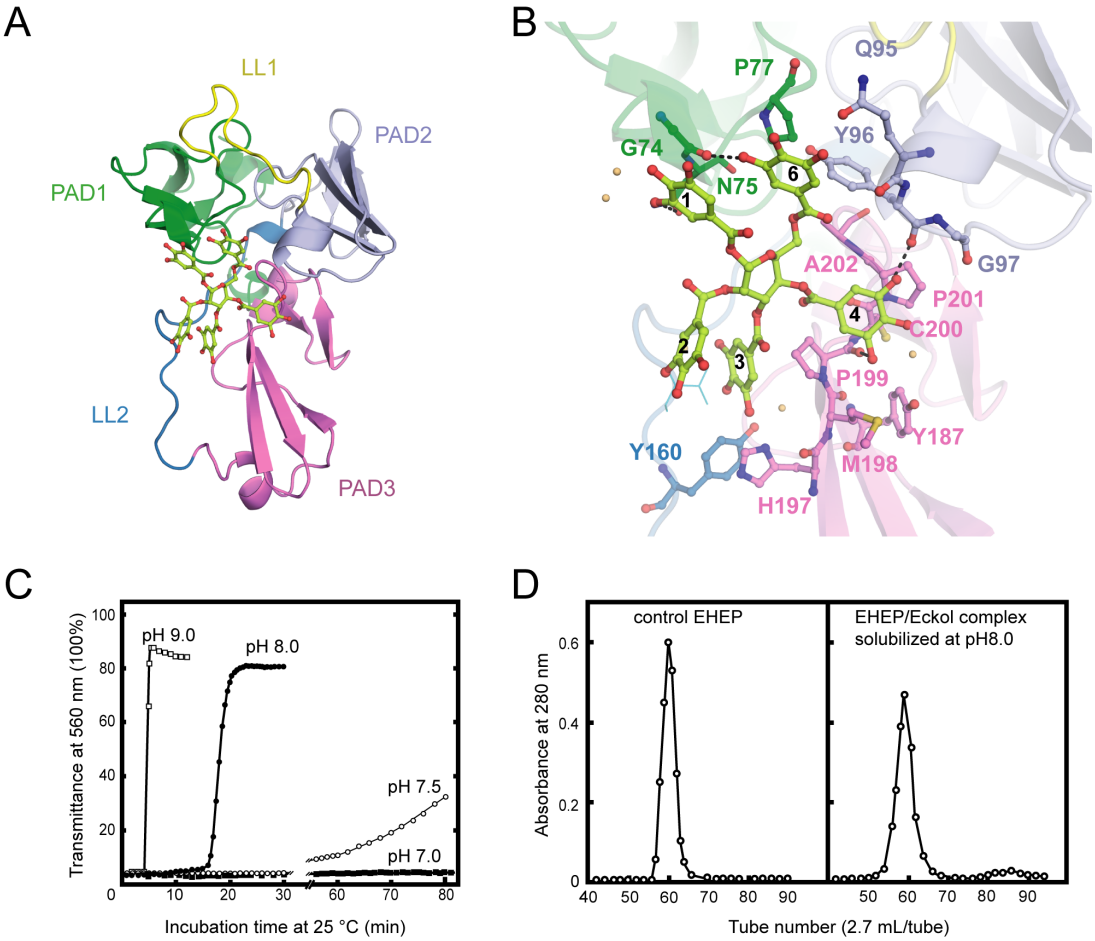

803

804

805 **Figure 3.** Structure of EHEP–TNA. (a) The overall structure of EHEP–TNA. (A) the
806 overall structure of EHEP–TNA. EHEP and TNA are shown by the cartoon and stick
807 model, respectively. EHEP is colored as in Fig. 1. The C and O atoms of TNA are
808 colored lemon and red, respectively. (B) Interaction of TNA (ball-stick in same color
809 as (A)) with EHEP (cartoon in same color as (A)) in EHEP–TNA structure. The
810 residues of EHEP in contact are labeled and shown by a ball-stick with N, O, and S
811 atoms in blue, red, and brown, respectively. The C and O atoms of TNA are colored the
812 same as (A), lemon and red, respectively. Dashed lines show hydrogen bonds. The
813 water molecules stabilizing TNA was shown as light orange spheres. (C) Effect of pH
814 on resolubilization of an EHEP–eckol precipitate. Buffers with pH 9.0, 8.0, 7.5, and 7.0
815 are presented as hollow square, solid circle, hollow circle, and solid square, respectively.

816 (D) The EHEP–eckol precipitate was dissolved in 50 mM Tris-HCl (pH 8.0) and
817 analyzed using a gel filtration column of Sephacryl S-100.
818

819 Fig 4

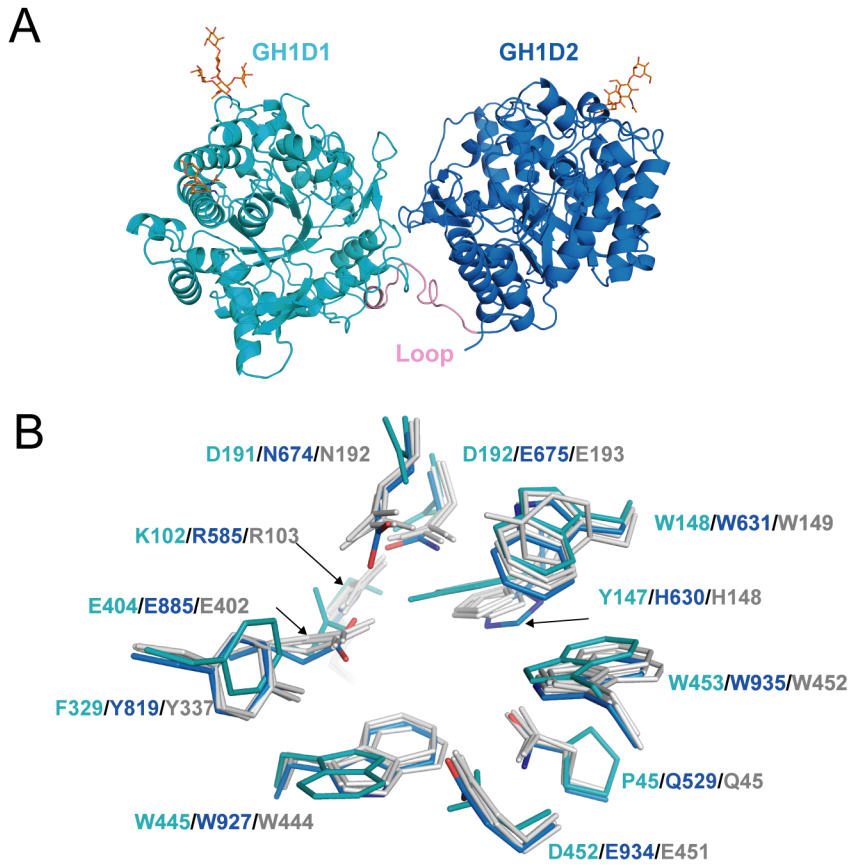

820

821 **Figure 4.** Structure of *aku*BGL. (A) Overall structure. The GH1D1 (light blue) and
822 GH1D2 (cyan) domains are linked by a long loop (linker-loop) colored in pink. The N-
823 linked glycans were shown in the orange stick. (B) Residues superposition of the GBS
824 and CR sites of the domains GH1D1 (cyan), GH1D2 (light blue) with β-glucosidase
825 structures from termite *Neotermes koshunensis* (*Nk*BGL, grey(PDB ID 3VIH) [32], β-
826 glucosidase from rice (*Os*BGL, gray, PDB ID 2RGL) [35], β-glucosidase from *Bacillus*
827 *circulans* sp. *Alkalophilus* (grey, PDB ID 1QOX) [67]. Only the residues numbers of
828 GH1D1 (cyan), GH1D2 (light blue), and *Nk*BGL (grey) are shown for clarity.

829

830 Fig 5

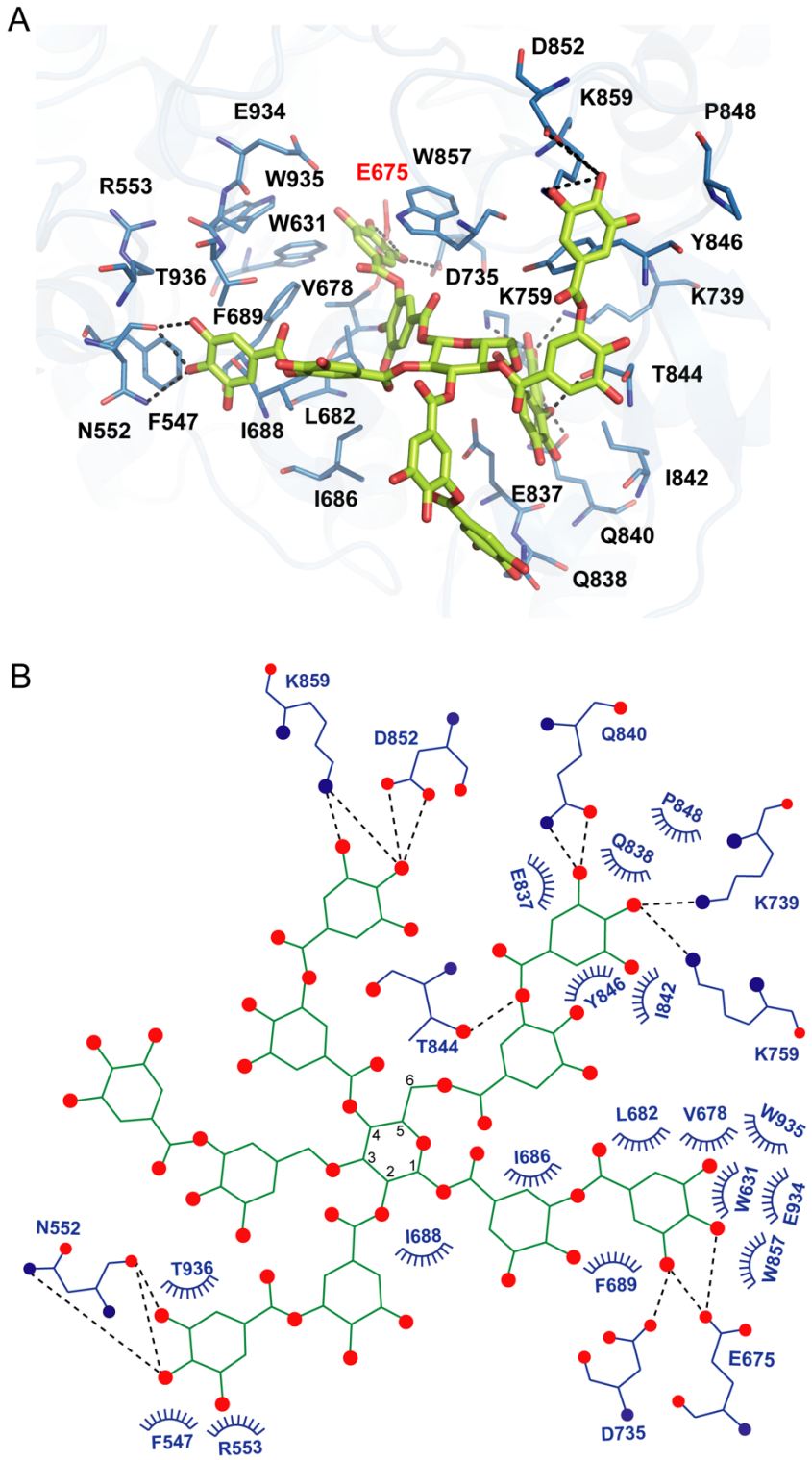

831

832 **Figure 5.** Docking model of *aku*BGL with TNA. (A) Detailed interaction between

833 *aku*BGL and TNA in the docking model. TNA is shown in the green stick model. The

834 hydrogen bonds are shown as dashed lines. (B) A 2D diagram of the interaction between

835 *aku*BGL and TNA shown in (A). The hydrogen bonds are shown as dash lines, and the

836 hydrophobic contacts as circular arcs.

837 Fig 6

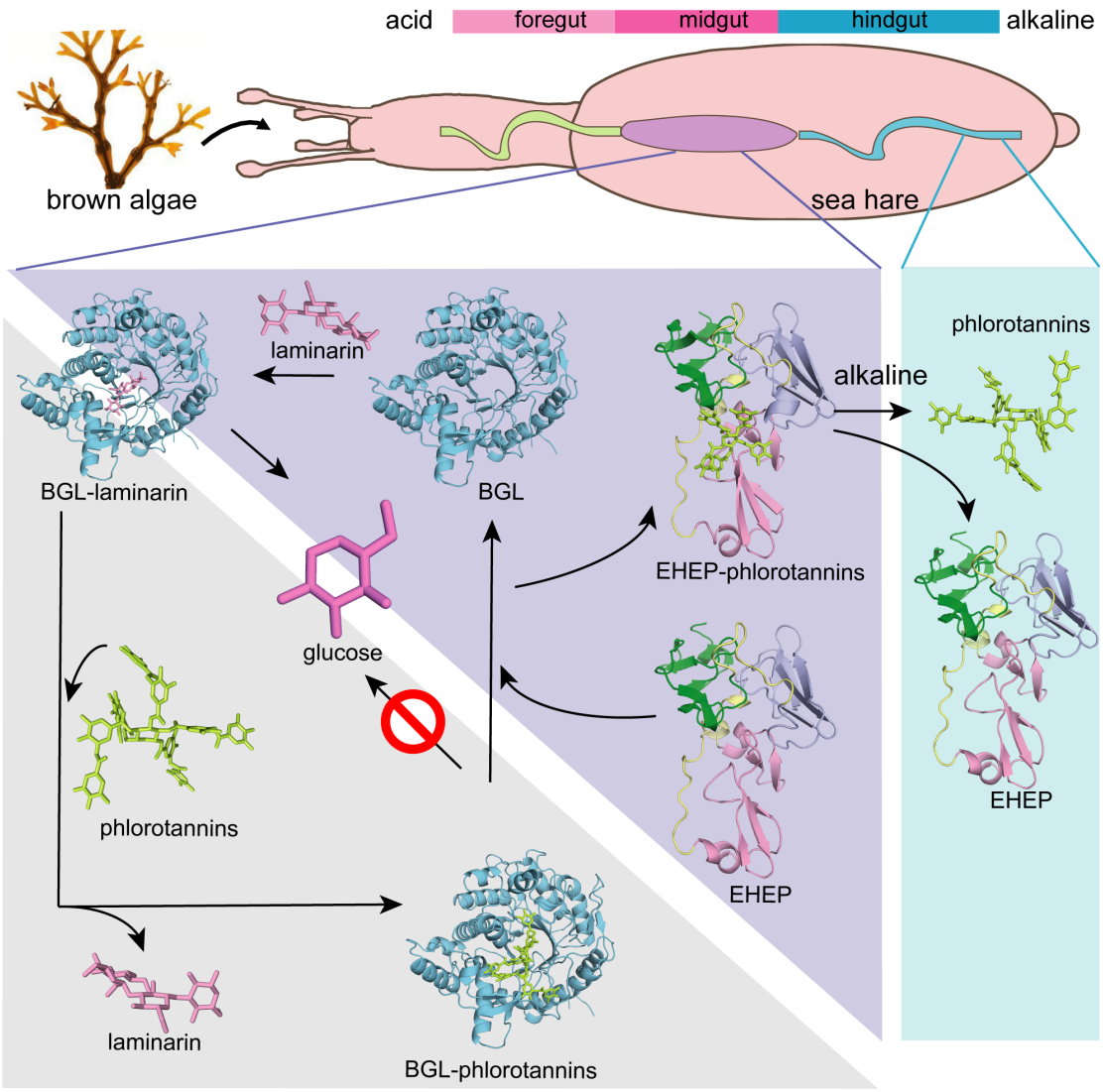

838

839 **Figure 6.** Proposed molecular mechanisms. Proposed molecular mechanisms of TNA
840 inhibition of *aku*BGL activity and EHEP's protective effects of *aku*BGL in *aku*BGL–
841 phlorotannin/laminarin–EHEP system (light purple triangle). The digestive tract of
842 *A.kurodai* consists of foregut (blue), midgut (purple), and hindgut (blue) (top). The bar
843 chart above depicts the pH of the digestive tract, with pink denoting acid and blue
844 denoting alkalinity.

845

Table 1 X-ray data collection and structure-refinement statistics.

	EHEP1	EHEP2	EHEP–TNA	*aku*BGL
Data Collection				
Beamline	PF BL17A	Spring 8 BL-41XU	PF BL17A	PF BL1A
Wavelength (Å)	0.9800	1.0000	0.9800	1.0000
Resolution range (Å)	46.56–1.15 (1.20–1.15)	47.02– 1.4 (1.45–1.4)	46.84–1.9 (1.97–1.9)	49.65–2.7 (2.80–2.7)
Space group	$P2_12_12_1$	$P2_12_12_1$	$P2_12_12_1$	$P6_2$
Unit-cell parameters *a, b, c* (Å)	42.2, 65.3, 66.5	40.6, 65.6, 67.5	42.5, 65.4, 67.2	91.7, 191.7, 12.6
Completeness (%)	93.4 (75.8)	99.30 (97.98)	99.9 (99.7)	99.9 (99.1)
Redundancy	6.6 (6.1)	6.4 (5.8)	6.4 (6.4)	10.7 (10.9)
Average I/σ(I)	19.28 (1.97)	14.34 (3.41)	15.39 (1.83)	10.69 (2.57)
R_{meas}(%)[a]	7.3 (90.5)	8.6 73.7(55.3)	8.9 (89.4)	19.4 (83.0)
$CC^{1/2}$ (%)	99.9（70.4）	99.8 (86.2)	99.9（73.7）	99.5 (84.2)
Molecules/ asymmetric unit	1	1	1	2
Refinement				
R_{work}[b]/R_{free}[c] (%)	18.19/18.91	16.57/18.39	19.87/23.54	18.39/21.98
No. of atoms	1955	1861	1732	15595
No. of residues	1600	1573	1580	15256
No. of water molecules	343	273	87	96
No. of Ligands	12	15	67	243
RMSD from ideality				
bond length (Å)	0.005	0.006	0.008	0.004
bond angle (°)	0.84	0.84	0.91	0.65
Ramachandran plot (%)				
Favoured	99.02	98.54	98.52	96.16
Allowed	0.98	1.46	1.48	3.74
Outliers	0.00	0.00	0.00	0.11
PDB accession code	8IN3	8IN4	8IN6	8IN1

The highest resolution shell is shown in parentheses.

[a] $R_{meas} = \Sigma_{hkl}\{N(hkl) / [N(hkl) -1] \}^{1/2} \Sigma_i|I_i(hkl)-< I(hkl)> | /\Sigma_{hkl} \Sigma_i|I_i(hkl)$, where where

$I_i(hkl)$ is the ith observation of the intensity of reflection *hkl* and $\langle I(hkl)\rangle$ is the mean over n observations.

[b]$R_{work} = \Sigma_{hkl}||F_{obs}(hkl)| - |F_{calc}(hkl)||/\Sigma_{hkl}|F_{obs}(hkl)|$.

[c]R_{free} was calculated with an approximate 5% fraction of randomly selected reflections evaluated from refinement.

855 **Supporting information**

856 **Fig. S1**

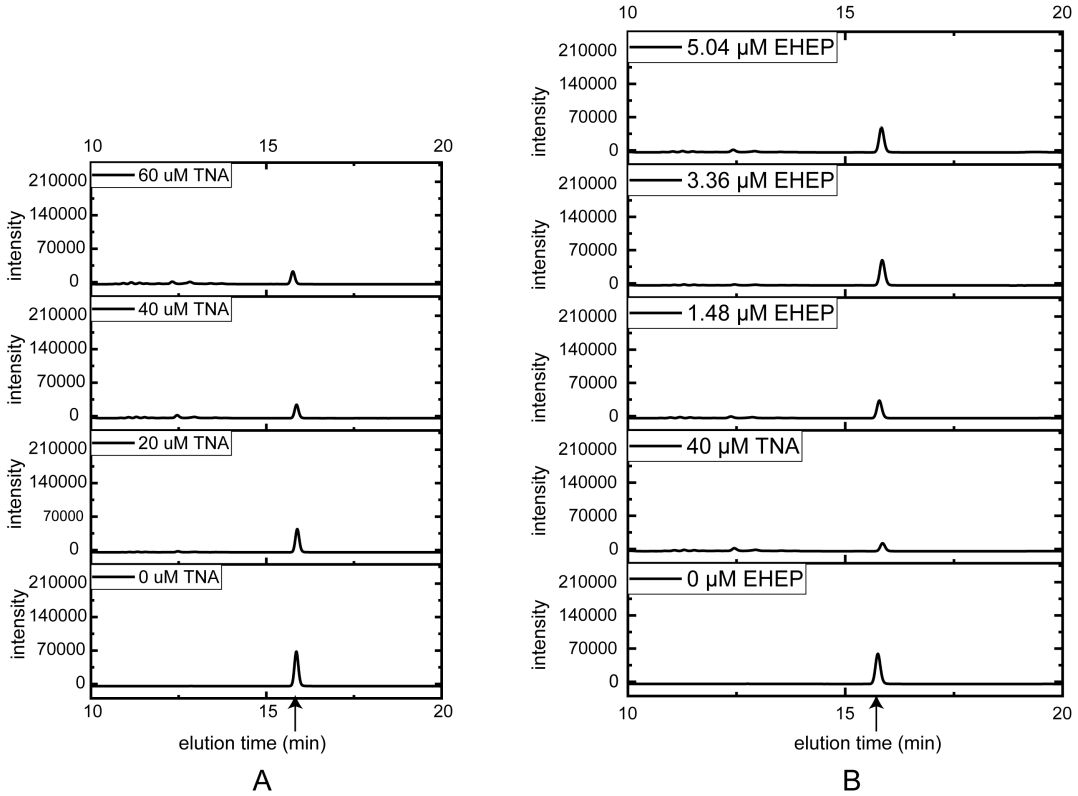

857 **Fig. S1.** HPLC profiles of *aku*BGL activity toward ortho-Nitrophenyl-β-galactoside.
858 (A) TNA inhibition *aku*BGL by increasing the concentration of TNA with 0.049 μM
859 *aku*BGL and 2.5 mM ortho-Nitrophenyl-β-galactoside. (B) EHEP protects *aku*BGL
860 from TNA inhibition by increasing the concentration of EHEP. The product peak was
861 marked by a black arrow.

862 Fig S2

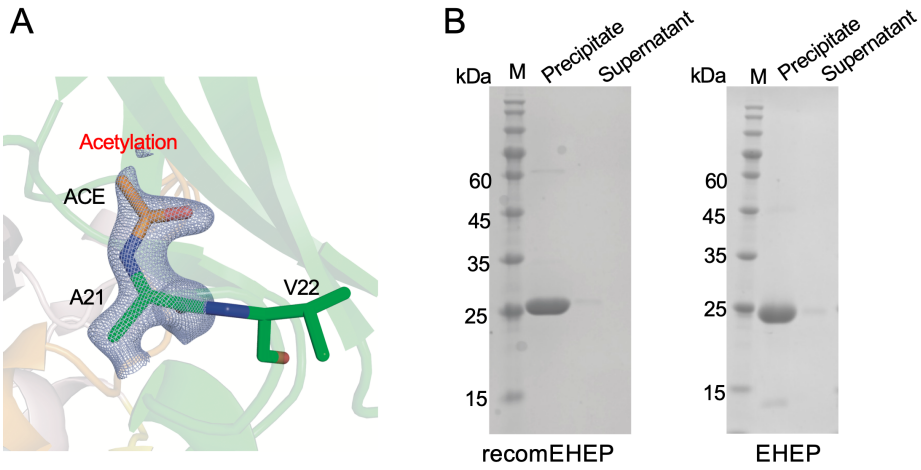

863

864 **Figure. S2**. (A) Acetylation modification on the N-terminal residue A21. The structure
865 is shown as sticks with an omitted map of the acetylation of A21 at a 3.3 σ level (blue-
866 white). (B) TNA binding activity of recomEHEP and EHEP. SDS–PAGE was run using
867 a mixture of recomEHEP/EHEP and TNA.

Fig.S3

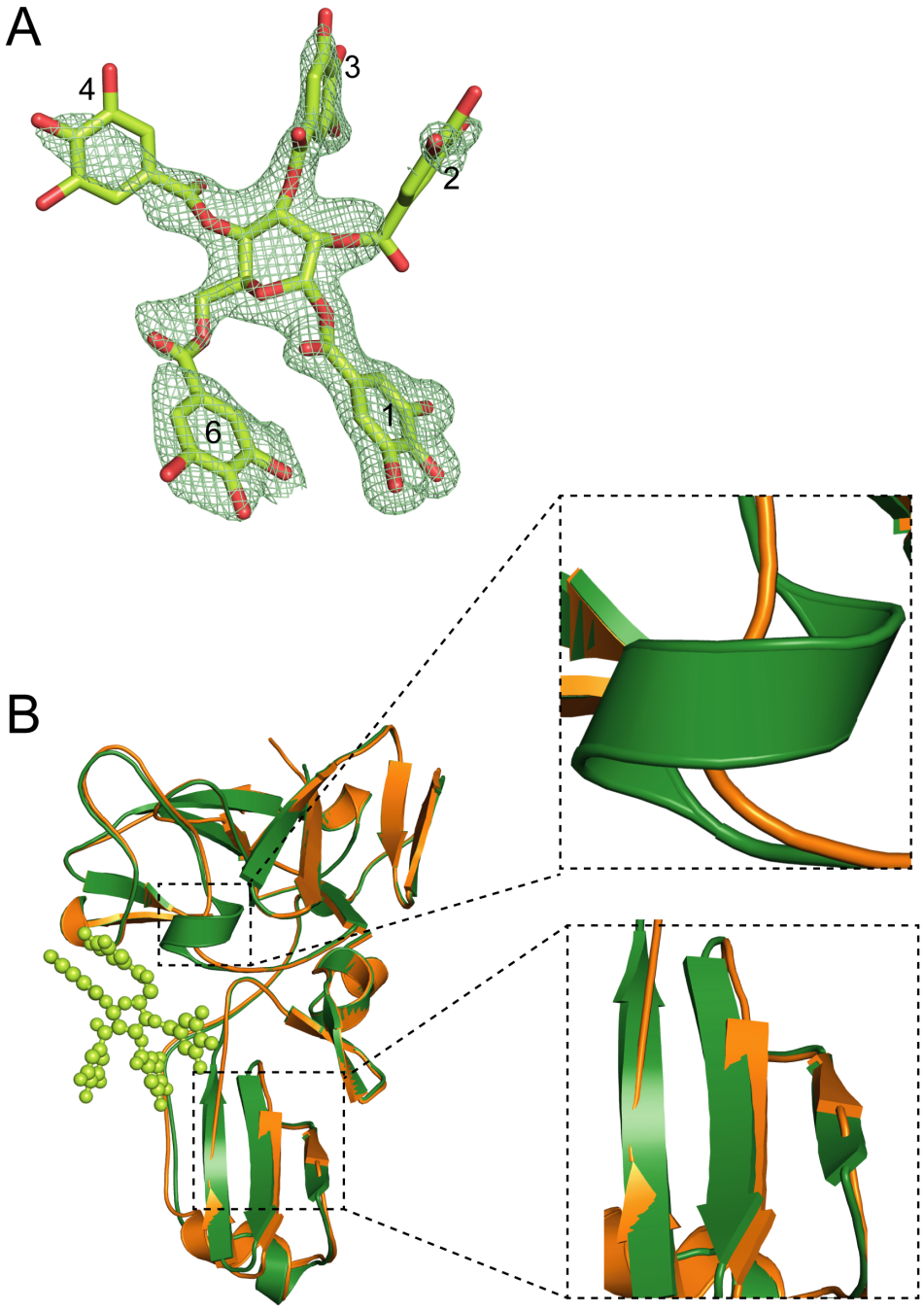

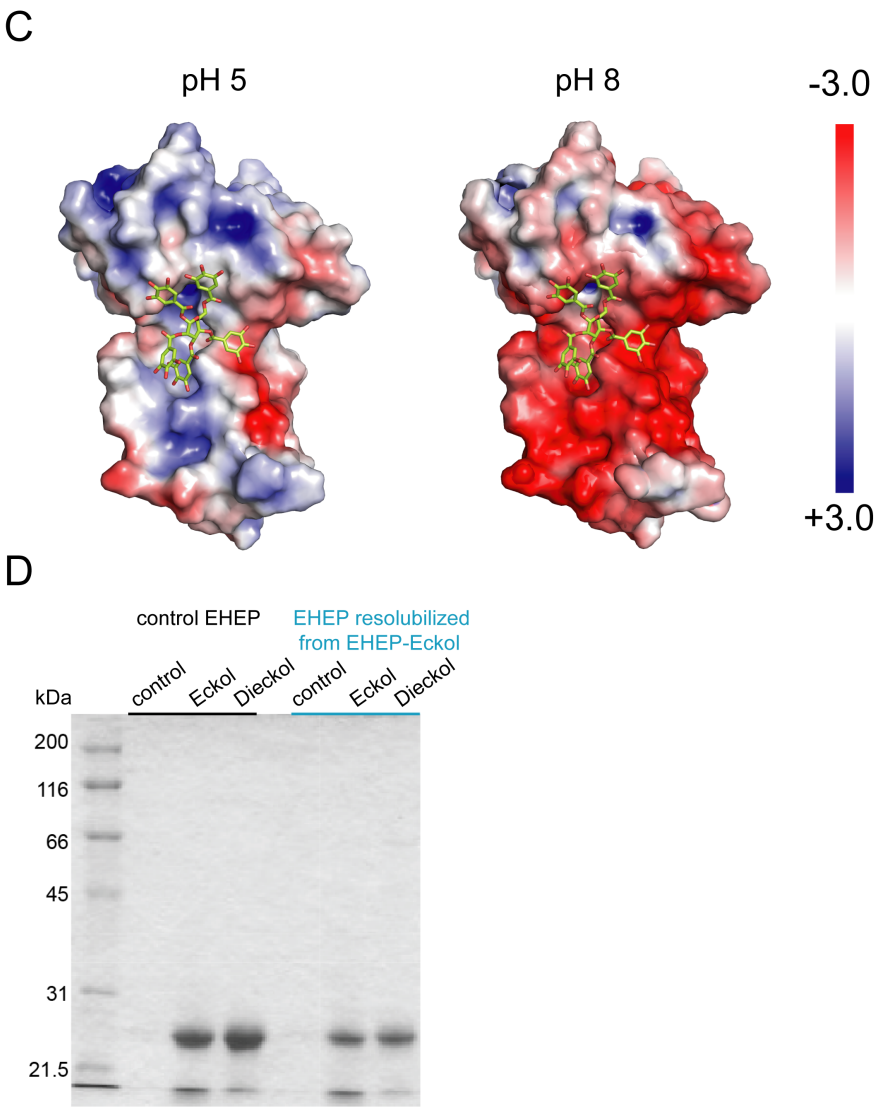

Figure S3. EHEP–TNA structure and structural comparisons. (A) TNA structure (stick model) in EHEP–TNA with an omitted map countered at the 2.0 σ level. The O and C atoms are colored red and lemon, respectively. (B) Structure superposition of apo EHEP (green) with EHEP–TNA (orange). The conformational changes are marked by black dotted boxes and zoomed on the right. (C) Electrostatic potential of the EHEP surface in the EHEP–TNA complex at different pH values, which were calculated using APBS-PDB2PQR software suite. (D) Activity of the resolubilized EHEP. The EHEP–eckol precipitate was resolubilized in Tris-HCl (pH 8.0) buffer and then the supernatant was purified using a Sephacryl S-100 HR column (2.0 ×110 cm) to measure eckol/dieckol -binding activity.

882 Fig.S4

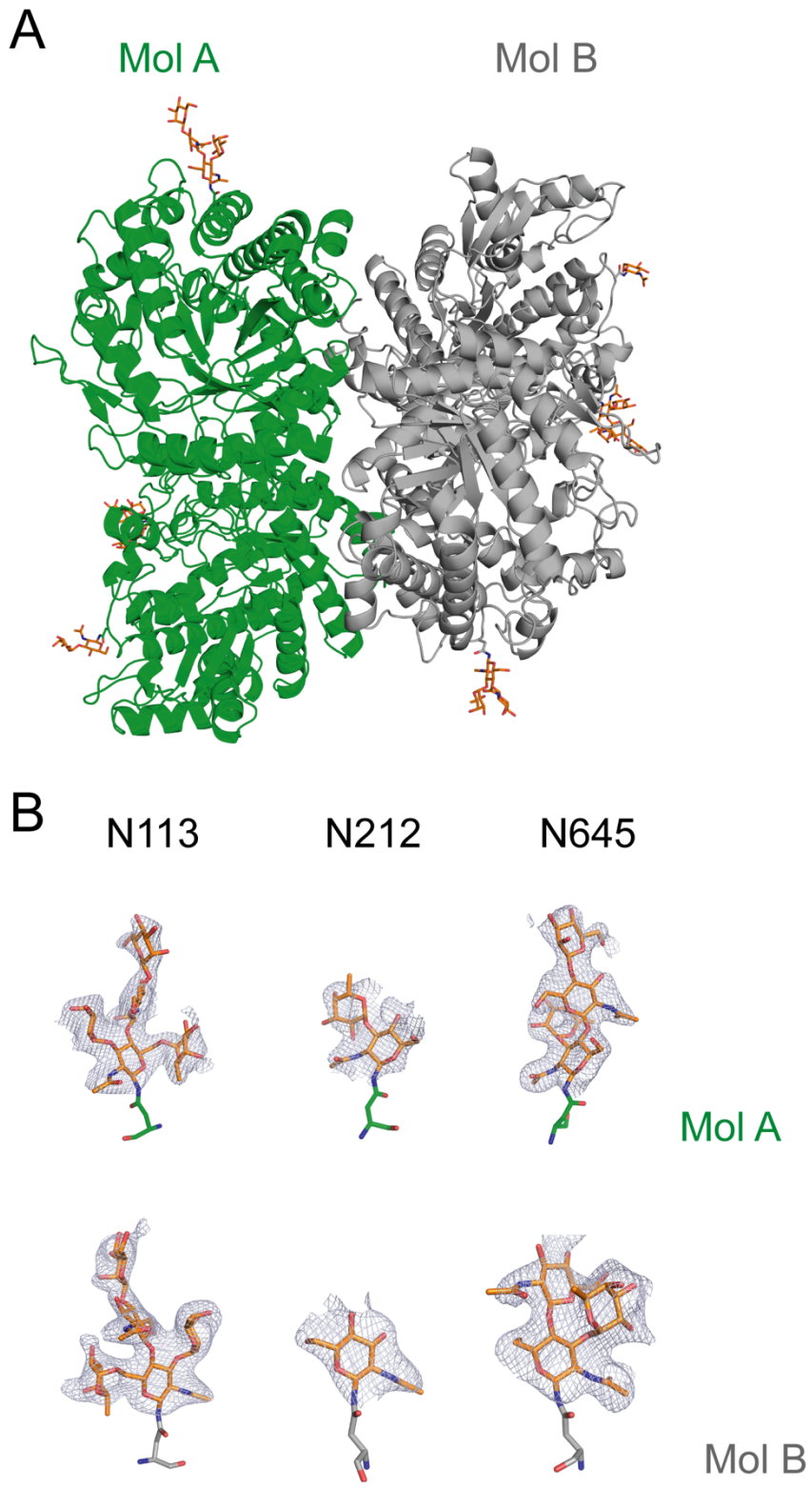

883

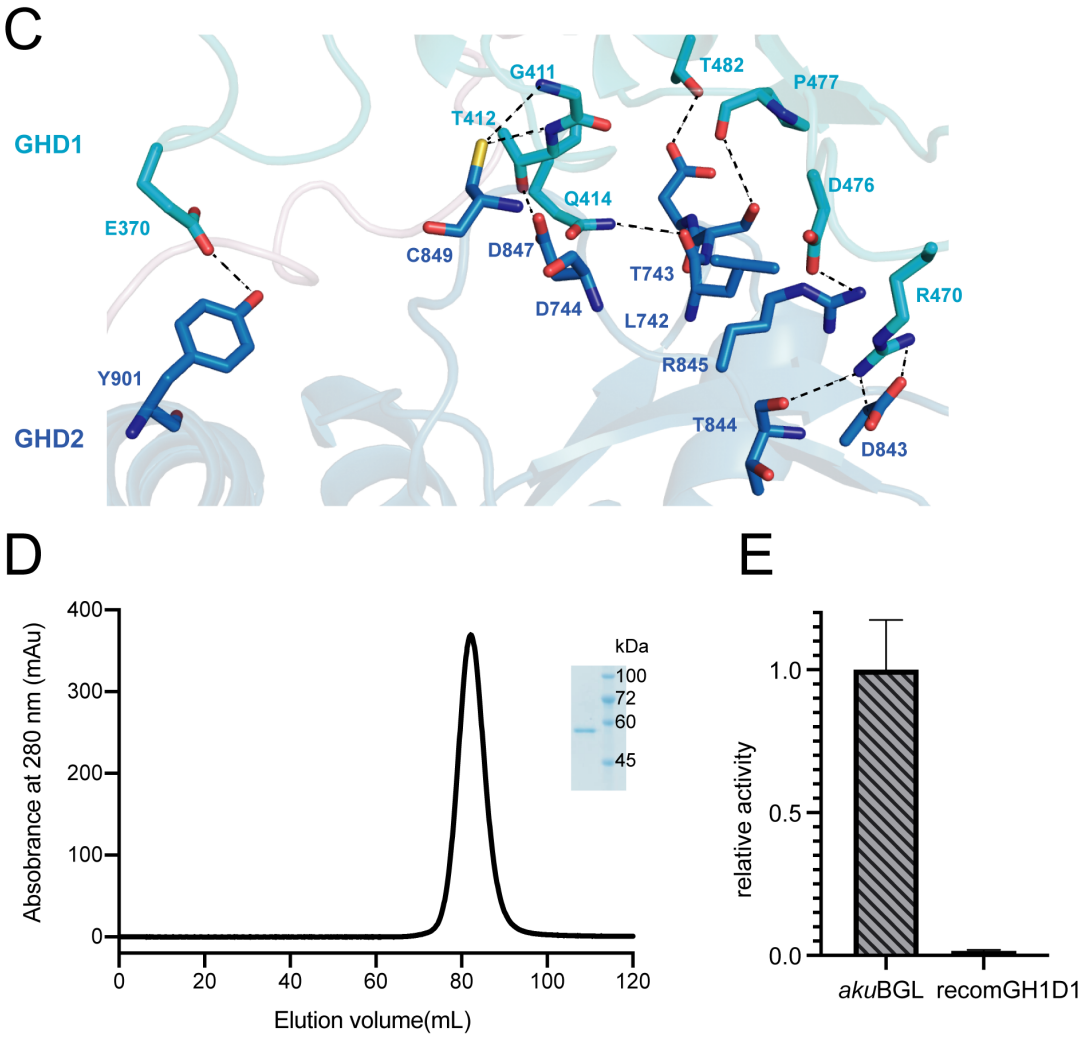

Figure S4. *aku*BGL structure. (A) Two *aku*BGL molecules in the asymmetric unit, colored green and grey, respectively. The glycosylation sites are shown as orange sticks, with O and N atoms in red and blue, respectively. (B) The glycosylation chains with omitted density maps are countered at the 2.0 σ level. (C) The interface between the GH1D1 (cyan) and GH1D2 (blue). The key interactions between the two domains are shown as black dashed lines. (D) Size exclusion chromatogram of the purified GH1D1 domain. The inset shows the SDS–PAGE analysis of the GH1D1 domain. (E) Galactoside hydrolytic activity of the recomGH1D1 toward ortho-Nitrophenyl-β-galactoside. The average and standard deviation of the relative activity were estimated from three independent replicates (N = 3).

895 Fig. S5

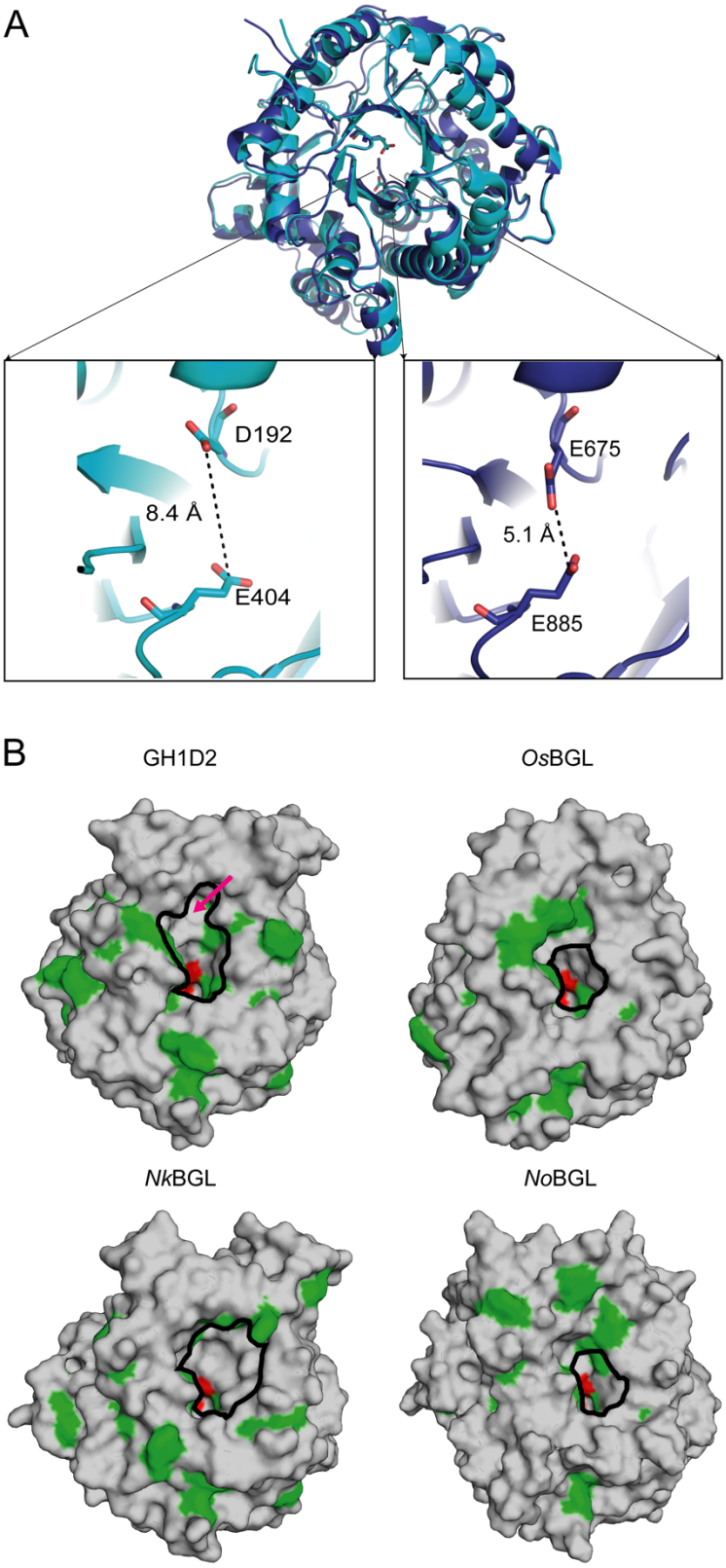

897

898 **Figure S5.** Structural comparison of BGLs. (A) Structure superposition of

899 GH1D1(cyan) and GH1D2 (blue). The enlarged picture shows the distance of
900 conceivable catalytic residues in GH1D1 and GH1D2. (B) Surface representations of
901 GH1D2, *Nk*BGL(PDB ID 3VIH) [32], *Os*BGL(PDB ID 2RGL) [35], and *No*BGL (PDB ID
902 5YJ7) [33] with the aromatic and catalytic residues colored green and red, respectively.
903 The red arrow indicates the location of the auxiliary site of GH1D2. The active pockets
904 are highlighted by a black circle on each surface.

905 **Fig. S6**

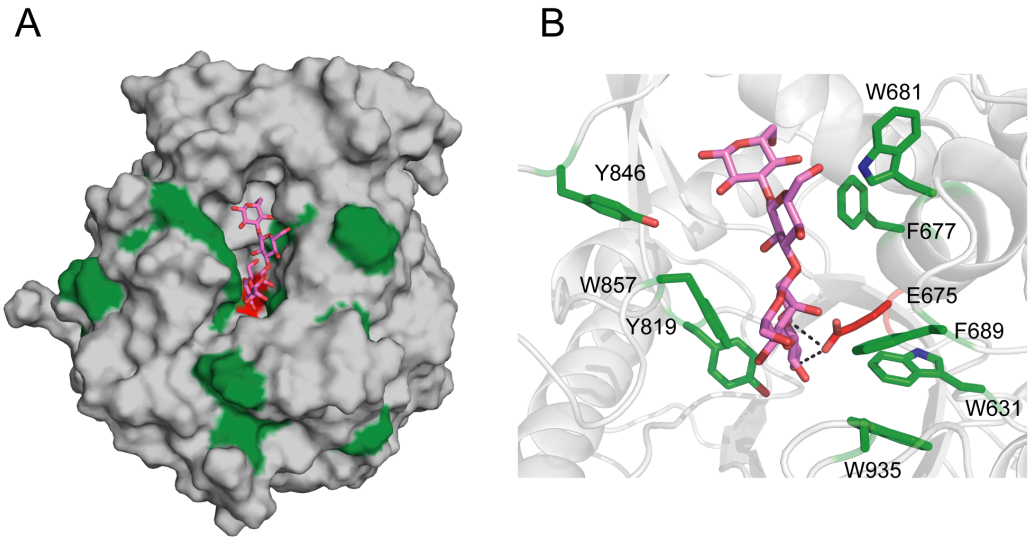

906

907 **Figure S6.** The model of GH1D2 docking with the substrate laminaritetraose. (A)
908 Overall model of GH1D2-laminaritetraose. GH1D2 is shown as a grey surface
909 representation and laminaritetraose as marine sticks. The aromatic and catalytic
910 residues of GH1D2 are colored green and red, respectively. (B) The closeup review of
911 interaction between laminatrtetraose and GH1D2 with key residues showing in sticks.

912

913 Fig. S7

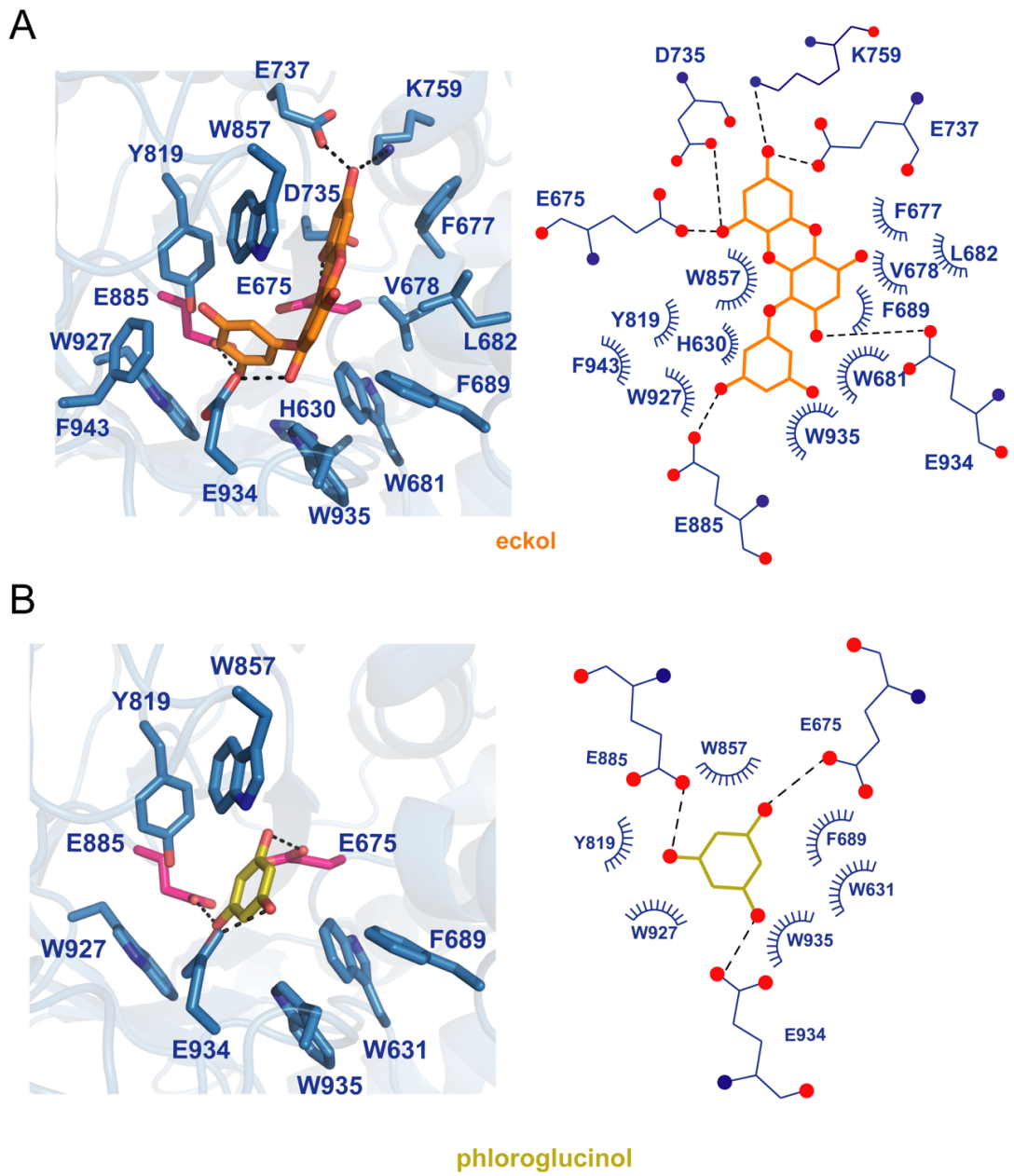

914

915 **Figure S7.** The models of GH1D2 docking. (A) With eckol, and (B) With
916 phloroglucinol. The left panel shows the 3D structures, and the right panel shows the
917 2D diagrams. The C, N, and O atoms of residues are colored light blue, dark blue, and
918 red, respectively. The C atoms of eckol and phloroglucinol are shown in orange and
919 yellow, respectively.